Observations of Reduced Turbulence and Wave Activity in the Arctic Middle Atmosphere Following the January 2015 Sudden Stratospheric Warming

Colin C. Triplett[1], **Jintai Li**[2,3], **Richard L. Collins**[2,3], **Gerald A. Lehmacher**[4], **Aroh Barjatya**[5], **David C. Fritts**[6], **Boris Strelnikov**[7], **Franz-Josef Lübken**[7], **Brentha Thurairajah**[8], **V. Lynn Harvey**[9], **Donald L. Hampton**[2], and **Roger H. Varney**[10]

[1]Space Sciences Laboratory, University of California, Berkeley, CA, USA

[2]Geophysical Institute, University of Alaska Fairbanks, Fairbanks, AK, USA

[3]Department of Atmospheric Sciences, University of Alaska Fairbanks, Fairbanks, AK, USA

[4]Department of Physics and Astronomy, Clemson University, Clemson, SC, USA

[5]Physical Sciences Department, Embry-Riddle Aeronautical University, Daytona Beach, FL, USA

[6]GATS Inc., Boulder, CO, USA

[7]Leibniz-Institute of Atmospheric Physics, University of Rostock, Kühlungsborn, Germany

[8]Center for Space Science and Engineering Research, Virginia Tech, Blacksburg, VA, USA

[9]Laboratory for Atmospheric and Space Physics, University of Colorado Boulder, Boulder, CO, USA

[10]Center for Geospace Studies, SRI International, Menlo Park, CA, USA

Abstract

Measurements of turbulence and waves were made as part of the Mesosphere-Lower Thermosphere Turbulence Experiment (MTeX) on the night of 25–26 January 2015 at Poker Flat

Research Range, Chatanika, Alaska (65°N, 147°W). Rocket-borne ionization gauge measurements revealed turbulence in the 70- to 88-km altitude region with energy dissipation rates between 0.1 and 24 mW/kg with an average value of 2.6 mW/kg. The eddy diffusion coefficient varied between 0.3 and 134 m^2/s with an average value of 10 m^2/s. Turbulence was detected around mesospheric inversion layers (MILs) in both the topside and bottomside of the MILs. These low levels of turbulence were measured after a minor sudden stratospheric warming when the circulation continued to be disturbed by planetary waves and winds remained weak in the stratosphere and mesosphere. Ground-based lidar measurements characterized the ensemble of inertia-gravity waves and monochromatic gravity waves. The ensemble of inertia-gravity waves had a specific potential energy of 0.8 J/kg over the 40- to 50-km altitude region, one of the lowest values recorded at Chatanika. The turbulence measurements coincided with the overturning of a 2.5-hr monochromatic gravity wave in a depth of 3 km at 85 km. The energy dissipation rates were estimated to be 3 mW/kg for the ensemble of waves and 18 mW/kg for the monochromatic wave. The MTeX observations reveal low levels of turbulence associated with low levels of gravity wave activity. In the light of other Arctic observations and model studies, these observations suggest that there may be reduced turbulence during disturbed winters.

Plain Language Summary

Turbulence remains an outstanding challenge in understanding coupling, energetics, and dynamics of the atmosphere. However, turbulence is recognized as a critical component in our models of terrestrial and space weather. Obtaining routine and accurate measurements of turbulence continues to be a major challenge. We present new rocket-borne measurements of turbulence in January 2015 at Poker Flat Research Range, Alaska. These rocket-borne measurements were coordinated with a suite of ground-based instruments. The rocket-borne instruments captured the small-scale structure of the turbulence. The ground-based measurements documented the meteorological and space weather conditions. We find low levels of turbulence coinciding with a disturbed atmosphere where wave activity is reduced. These finding suggest that there may be systematically low levels of turbulence in the Arctic middle atmosphere, as the Arctic middle atmosphere is routinely disturbed in winter.

1. Introduction

Observations of downward transport of nitrogen oxides (i.e., NO$_X$ = NO+ NO$_2$) from the thermosphere into the stratosphere during the Arctic winter have highlighted how meteorological processes control of the impacts of energetic particle precipitation events in the atmosphere (López-Puertas et al., 2006; Mironova et al., 2015; Randall et al., 2006). While this transport is observed in all winters, it is enhanced (with NO$_X$ concentrations up to 50 times higher than usual) in winters where sudden stratospheric warming (SSW) events disrupt the polar stratospheric vortex (Randall et al., 2009). The transport of NO$_X$ coincides with the recovery phase of the polar vortex, when the vortex initially reforms in the mesosphere and descends into the stratosphere. These observations have prompted studies with contemporary whole atmosphere models to assess the relative importance of different transport processes (i.e., advection, eddy diffusion, and molecular diffusion; Meraner & Schmidt, 2016; Smith et al., 2011). However, sensitivity studies with these models have

shown that changes of a factor of two in the eddy diffusion coefficients yield significant changes in the transport of minor species (Garcia et al., 2014; Meraner & Schmidt, 2016). These models represent eddy diffusive transport by a diffusion coefficient where the values of the eddy diffusion coefficient, K, vary between 10 and 100 m^2/s in the mesosphere and lower- thermosphere (MLT, ~60–110 km; Garcia et al., 2014; Meraner & Schmidt, 2016; Smith et al., 2011). Satellite observations of carbon dioxide (CO_2) and atomic oxygen (O) in the MLT have yielded global-mean estimates of the eddy diffusion coefficients that are consistent with the model values (Salinas et al., 2016; Swenson et al., 2018).

However, measurements of density fluctuations or expansion of chemical released trails have reported that higher values of turbulent energy dissipation and eddy diffusion occur in altitude regions of convective and/or dynamic instability (e.g., Bishop et al., 2004; Lehmacher et al., 2006, 2011; Lehmacher & Lübken, 1995; Strelnikov et al., 2017; Szewczyk et al., 2013). Turbulence is generated by local wave-driven instabilities (e.g., Becker, 2012; Fritts et al., 2017, 2018; Fritts & Alexander, 2003; Hines, 1988; Sutherland, 2010). Regions of convective instability, where the temperature gradients are negative and adiabatic or superadiabatic (i.e., adiabatic or superadiabatic lapse rates), are often found on the topside of mesospheric inversion layers (MILs). MILs are layers of increasing temperature in the mesosphere that represent a departure from the expected negative temperature gradient (see review by Meriwether & Gerrard, 2004). Breaking planetary waves, tides, and gravity waves have all been shown to generate MILs (Liu et al., 2000; Liu & Meriwether, 2004; Salby et al., 2002; Sassi et al., 2002). The presence of a persistent adiabatic negative temperature gradient on the topside of the MILs is consistent with a well-mixed turbulent layer (Whiteway et al., 1995). Turbulence has been observed coincident with these adiabatic gradients (Collins et al., 2011; Lehmacher et al., 2006; Lehmacher & Lübken, 1995; Szewczyk et al., 2013; Thomas et al., 1996). These studies have reported values of the energy dissipation rate, ε, that are 1–100 mW/kg in the upper mesosphere (~60–95 km) and increase to 100–1,000 mW/kg in the lower thermosphere (~90–105 km). The corresponding values of K are 1–100 and 100–1,000 m^2/s, respectively. Reconciling these observed values of turbulent dissipation and diffusion with the values used in model studies remains an area of active research (e.g., Fritts et al., 2018; Meraner & Schmidt, 2016; Smith, 2012). The situation is further complicated by the fact that eddy diffusion in models represents transport due to all subgrid scale processes that include wave transport as well as turbulence (e.g., Grygalashvyly et al., 2011; Guo et al., 2017; Smith, 2012; Walterscheid, 2001).

Despite these challenges, measurements of turbulence in the Arctic have shown systematic behavior. Rocket-based measurements of neutral density fluctuations with ionization gauges report seasonally averaged turbulent energy dissipation rates that are an order of magnitude lower in winter (10–20 mW/kg) than summer (150 mW/kg; Lübken, 1997; Lübken et al., 2002). Measurements during the spring transition show increases in turbulent energy dissipation within a period of weeks consistent with rapid changes in the seasonal winds and expected gravity wave activity (Müllemann et al., 2002). However, these turbulent studies did not include measurements of the gravity wave activity. In this paper we present new wintertime observations of turbulence and waves in the Arctic middle atmosphere. These observations were made as part of the Mesosphere-Lower Thermosphere Turbulence

Experiment (MTeX) that was designed to investigate systematic relationships between turbulence in the MLT, instabilities in the MLT, and gravity waves propagating through the stratosphere and mesosphere. MTeX consisted of rocket-borne in situ ionization gauge measurements of turbulence and plasma conditions with ground-based measurements of the meteorological conditions and plasma conditions. Ground-based Rayleigh and resonance lidars characterized gravity wave activity and instabilities. The MTeX turbulence measurements were made following the detection of a MIL by the ground-based Rayleigh lidar. In section 2 we describe the instruments, techniques, and methods used to detect and characterize turbulence and waves. In section 3 we present the MTeX observations. In section 4 we analyze the relationships between the waves and turbulence and compare the MTeX measurements to other Arctic measurements. In section 5 we present our summary and conclusions.

2. Data and Methodology

2.1. MTeX Vehicles and Trajectories

MTeX was conducted at Poker Flat Research Range (PFRR), Chatanika, Alaska (65°N, 147°W) on the night of 25–26 January 2015 after the January 2015 SSW when the atmosphere remained disturbed (Manney et al., 2015). The MTeX investigation consisted of in situ density and plasma measurements made by two rocket payloads that were launched 33 min apart just after local midnight at 0013 LST and 0046 LST on 26 January 2015 (0913 and 0946 UT, UT = LST + 9 hr). The MTeX launch vehicles were Terrier-Malemute rockets (National Aeronautics and Space Administration code 46) and identified as 46.009 and 46.010 respectively. Photographs of the MTeX payloads and launches have been previously published (Collins et al., 2015). The payloads were designed to yield measurements over altitudes from 70 to 120 km on both the upleg and downleg of their trajectories. The payloads were reoriented near apogee so that the front of the payloads were oriented in the ram direction on the downleg as well as the upleg. We present the MTeX payload trajectories in Figure 1. In this study we present results from the upleg and downleg of 46.009 and downleg of 46.010.

2.2. CONE Ionization Gauge

The Combined Sensor for Neutrals and Electrons (CONE) ionization gauge (ion gauge) has been used to make density measurements in the middle atmosphere since the 1990s (Giebeler et al., 1993; Rapp et al., 2001; Szewczyk et al., 2013). The CONE instrument consists of a sensor and an electronics package. The CONE sensor is an ion gauge surrounded by a shielding grid and a fixed-bias electrostatic probe that was mounted on the front of the payload. The primary measurement is the electrometer current. For the MTeX investigation the CONE electronics package was redesigned and constructed using contemporary programmable logic devices. The upgrade resulted in measurements with higher sensitivity, reduced noise, and a higher sampling rate than previous measurements. The CONE sampling rate was 5,208 samples per second (sps). The CONE current profile was measured in five ranges, where the electronic gain of the instrument increased by successive orders of magnitude as the atmospheric density decreased, to maintain a constant dynamic range in the signal. We plot the CONE electrometer current recorded by payload

46.009 during the upleg in Figure 2. The gain switching yields characteristic discontinuities in the measured current profile. At the highest altitudes (and lowest densities) the CONE profile is constant due to a small constant current. The retrieval of the density profile from the CONE current profile is conducted in four steps (Triplett, 2016). In the first step we calculate a continuous CONE profile by binning the 192 μs samples at 50 ms corresponding to the timing of the trajectory recording. We correct the CONE current profile for the change in gain and remove the background current by assuming continuity across the discontinuities and fitting the logarithm of the signal to a third-order polynomial. This process is iterated to estimate the change in gain at each range and subtract the constant current scaled by the gain from the signal at all ranges. In the second step we correct the continuous CONE profile for aerodynamic ram effects using the density profile derived from the Rayleigh lidar signal. In the third step we fit a third-order polynomial to the logarithm of the density profile. The density is then reconstituted by taking the exponential of the sum of the polynomial and the residual of the polynomial (smoothed at 2 km). The statistical relative uncertainty in the resultant density is 0.2%. In the final step we determine the absolute density by normalizing the Rayleigh lidar density profile to the local National Weather Service radiosonde measurement profile and then normalizing the CONE density profile to the Rayleigh lidar density profile. The CONE measurements yielded density and temperature measurements every 50 ms (corresponding to ~50 m). We plot the density profile derived from the CONE measurements on the upleg of payload 46.009 in Figure 3. We also plot the corresponding density profile measured by the Rayleigh lidar and from the Mass Spectrometer Incoherent Scatter (MSIS) model (Hedin, 1991; Papitashvili, 2016). The lidar profile represents the average of a 2-hr measurement around the CONE measurement. The uncertainties in the Rayleigh lidar and the MSIS profiles are discussed further below. The density measured by CONE differs from the density measured by the lidar by 6% at 90 km, which is less than the uncertainty in the lidar measurement. The density measured by CONE is larger than the MSIS model density by 20% at 90 km, which is more than the 10% uncertainty in the MSIS density. We calculate a temperature profile over the 70 to 120 km altitude range from the CONE density profile. We adapt the standard retrieval methods to allow for the fact that the composition of the atmosphere, and thus, the mean molecular mass of air decreases with altitude in the thermosphere due to increases in the concentration of atomic oxygen (O). We use MSIS to both estimate the mean molecular mass and provide an initial temperature at 120 km for the retrieval (Triplett, 2016). The statistical uncertainty in the temperature is less than 0.5 K. We calculate the square of buoyancy frequency, N^2, from the temperature profile using established relationships (e.g., Dutton, 1988). The statistical error in N^2 is less than 5 $\times 10^{-5}$ s^{-2}.

The CONE instrument also yields measurements of density fluctuations every 192 μs (corresponding to ~20 cm). The turbulent energy dissipation rate is determined from the spectrum of the fluctuations over 1-s intervals following established methods based on spectral fitting of a Heisenberg model spectrum to identify the frequency at the transition between the inertial subrange and the viscous subrange of the spectrum (Lübken, 1992, 1997; Lübken et al., 1993; Szewczyk, 2015). This transition frequency, f_0, corresponds to the inner wave number and the inner scale, l_0, of the turbulence and is directly related to the energy dissipation rate, ε. The spectral fits are subject to three consistency checks: first that

the transition frequency lies between the maximum and minimum significant frequencies in each spectrum, second that the inner and outer wavenumbers of the spectral fit are mutually consistent, and third that the spectral fit encompasses over 50% of the energy of the fluctuations (Triplett, 2016). The spectral fit also yields an uncertainty estimate in the inner wave number and hence the inner scale and energy dissipation rate. We plot an example spectrum from the upleg of payload 46.009 in Figure 4. We see that the fluctuation signal extends to 30 Hz, and at higher frequencies it is dominated by noise. The signal-to-noise ratio of the spectrum over the fitting range is 10^4. We summarize the characteristics of the measurement, background atmosphere, and turbulence associated with this spectrum in in Table 1. We determine the energy dissipation rate from the inner scale, and then we determine the outer scale, L_B, from the energy dissipation rate (Lübken, 1997). We calculate the root-mean-square (RMS) fluctuations over the 3 to 30 Hz range to avoid contamination by spin modulation at 2 Hz and to include only those frequencies that are signal dominated. We calculate the heating rate from the energy dissipation rate using the specific heat capacity of air. We calculate the eddy diffusion coefficient, K, from the turbulent dissipation rate, ε, using the relationship,

$$K = 0.81 \times \frac{\varepsilon}{N^2} \quad (1)$$

where N is the buoyancy frequency (Weinstock, 1978). This relationship has been widely used to determine K from ε and vice versa (e.g., Bishop et al., 2004; Collins et al., 2011; Lübken, 1997).

2.3. Langmuir Probe

Each MTeX payload included four plasma density probes. These were a fixed-bias direct current (DC) multi-surface Langmuir probe (mDCP), a sweeping impedance probe (SIP), a sweeping Langmuir probe (SLP), and a multi-needle Langmuir probe (mNLP; Blake, 2014; Blix et al., 1990; Steigies & Barjatya, 2012; Strelnikov et al., 2017). The SIP yielded absolute measurements of the plasma density. The mDCP yielded relative measurements of the plasma density that were then normalized to the SIP. During the MTeX flights the SLP and mNLP were saturated by the auroral ionization and did not yield plasma density profiles. The mDCP measurements were sampled at 5 sps and yielded measurements at approximately 20-cm resolution. However, there are harmonics in the data from 2.5-Hz spin modulation, and interference from the SLP (9 Hz) and SIP (20 Hz). We filter the mDCP profile to remove these effects. We report the electron density profiles and gradients that we derive from the mDCP and SIP measurements. The instrument noise within the Langmuir probe results in an error of 2×10^8 m^{-3} in the electron density.

2.4. Rayleigh and Resonance Lidars

Rayleigh lidar measurements have been made at Chatanika on an ongoing basis since 1997 and yielded measurements of temperature and density profiles in the upper stratosphere and mesosphere (40–80 km; e.g., Collins et al., 2011; Irving et al., 2014; Triplett et al., 2017). The Rayleigh lidar was operated over a 13-hr period from 1827 LST until 0715 LST (0327–

1615 UT). The lidar transmitter included a Nd:YAG laser operating at 532 nm and 20 pulses per second (pps) with an average power of 7 W. The Rayleigh lidar system was extended in two ways for the MTeX investigation. First, the original receiver telescope of diameter 0.6 m was replaced with a telescope of diameter 1.04 m. Second, the receiver was extended from a single-channel to a two-channel system (Triplett, 2016). The two-channel receiver system had a high-altitude channel that received 94% of the total lidar signal and a low-altitude channel that received 6% of the total lidar signal. The high-altitude channel signals were a factor of three greater than the single-channel system (Collins et al., 2011). The increase in signal in the high-altitude channel reduces the uncertainty in the lidar signals and extends the measurements of density and temperature to higher altitudes than in previous studies. The decrease in signal in the low-altitude channel reduces the effects of pulse pile-up and extends the measurements of density and temperature to lower altitudes than in previous studies. The high-altitude lidar signal is used above 61 km and the low-altitude lidar signal below 61 km. We used the rocket-borne CONE measurements of temperature as the initial temperature at the upper altitude for the high-altitude signal and thus remove this source of uncertainty from the lidar measurements. We then used the temperature determined from the high-altitude lidar signal as the initial temperature for the low-altitude lidar temperature retrieval. The temperature profiles are also used to determine the potential temperature by integrating upward from 61 km assuming the temperature and potential temperature are equivalent at that altitude (Franke & Collins, 2003). The resolution of the Rayleigh lidar measurements was 50 s and 48 m. The Rayleigh lidar measurements yield nightly average temperature and density profiles over the 35- to 100-km altitude range, temperature, and density profiles at 15-min intervals and 120-min integration (termed 2 hr) over the 35- to 92.5-km altitude range, and density profiles at 5-min intervals and 30-min integration (termed 30 min) over the 35- to 77-km altitude range. The statistical errors increase from 0.1 to 8 K and from 0.3 to 9 K for the nightly average and 2-hr temperature profiles, respectively. The statistical relative errors increase from 0.06% to 2.7%, from 0.2% to 3.7%, and from 0.3% to 2.8% for the nightly average, 2 hr, and 30-min density profiles, respectively.

We determined the gravity wave activity in the stratosphere and mesosphere from the Rayleigh lidar temperature and density profiles. We used established techniques to determine the density fluctuations in altitude and time and hence calculate the RMS density fluctuations and the specific potential energy of the gravity waves (Thurairajah, Collins, Harvey, Lieberman, & Mizutani, 2010; Thurairajah, Collins, Harvey, Lieberman, Gerding, et al., 2010; Triplett et al., 2017). The RMS density fluctuations are determined from the 30-min density profiles over a given altitude range. The fluctuations are high-pass filtered in time remove components with periods longer than 4 hr and so represent gravity waves with periods between 1 and 4 hr (with a geometric mean period of 2 hr). The fluctuations are low-pass filtered at 2 km and so represent gravity waves with vertical wavelengths between 2 km and a maximum determined by the altitude range. The RMS displacement and specific potential energy are then determined using the buoyancy frequency determined from the average temperature profile. We detected monochromatic waves in the density profiles by determining the best temporal harmonic fits to the density fluctuations at each altitude and then determining the vertical phase progressions to the harmonic fits. We fitted harmonics to

the 2-hr density profiles to find waves with periods greater than 2 hr and conducted fits to the 30-min data to find waves with periods between 1 and 4 hr. We determined the vertical wavelength from the observed frequency and vertical phase progression and then used the gravity wave polarization and dispersion relationships to estimate the horizontal wavelength, horizontal phase speed, group velocity, RMS horizontal velocity, vertical displacement, and specific potential energy (Hines, 1960).

Sodium resonance lidar measurements have been made at Chatanika on an ongoing basis since 1995 and yielded measurements of the sodium layer profile in the upper mesosphere and lower thermosphere (e.g., Collins & Smith, 2004; Gelinas et al., 2005). The sodium resonance lidar was operated over an 11-hr period from 2008 LST until 0716 LST (0508–1616 UT). This lidar system is similar to one that was operated during the Turbopause investigation (Collins et al., 2011; Lehmacher et al., 2011). The excimer-pumped dye laser used in the Turbopause investigation was replaced with a Nd:YAG pumped dye laser (Martus, 2013). The Nd:YAG pumped dye laser operated at 589 nm and 10 pps with an average power of 0.25 W. We used the same standard inversion methods as used in previous studies to determine the sodium concentration profiles between 70 and 120 km. We then combined the sodium concentration profiles with the density profiles measured by the Rayleigh lidar to determine the sodium mixing ratio profiles. The resolution of the resonance lidar measurements was 100 s and 75 m. The sodium resonance lidar measurements yielded sodium concentration profiles at 15-min intervals and 60-min integration. The statistical relative errors in the sodium concentrations are less than 6% in the 80- to 100-km altitude range.

2.5. PFISR, All-Sky Imager, and Magnetometer

The Poker Flat Incoherent Scatter Radar (PFISR) has been operating at PFRR since 2007 (Heinselman & Nicolls, 2008). PFISR is a multibeam phased array radar. During the MTeX investigation the radar operated with four beams to yield measurements of the electron density and the electric field. The measurements of the electron density profile from three beams were interpolated to yield a measurement of the electron density profile along the upleg of the MTeX flight path. The radar employed an alternating pulse code to yield electron density measurements between 90 and 300 km with 56-m and 300-s resolution. A multispectral All-Sky Imager (ASI) is operated at PFRR and provides high-resolution all-sky images of the aurora at 630, 558, and 428 nm (e.g., Lyons et al., 2015). The ASI operated from evening twilight until morning twilight (1712–0851 LST, 0212–1751 UT). ASI imagery is made available as movies at 13-s resolution (Hampton, 2017a). A three-axis fluxgate magnetometer is also operated at PFRR and provides measurements of the three components of magnetic field and geomagnetic activity (e.g., Collins et al., 1996). The magnetometer measurements are made at 1 sps (Hampton, 2017b).

2.6. MERRA-2, SABER, and MSIS

The Modern-Era Retrospective Analysis for Research and Applications version 2 (MERRA-2) reanalysis data set describes the meteorological conditions in the troposphere, stratosphere, and mesosphere from 1980 to the present (Bosilovich et al., 2015; Gass, 2016; Molod et al., 2015). MERRA-2 assimilates temperature and ozone measurements from the

Microwave Limb Sounder (MLS) above 5 hPa beginning in August 2004. This results in more realistic synoptic meteorology in the upper stratosphere and lower mesosphere than in other reanalysis data sets (Fujiwara et al., 2017; Gelaro et al., 2017). We use the MERRA-2 data to characterize the daily winds over Chatanika. We report MERRA-2 median wind profiles over the 2005–2018 period that assimilates MLS. We also use the MERRA-2 data to characterize the mesoscale imbalance in the flow (Plougonven & Zhang, 2014). We calculate the residual in the nonlinear balance equation to characterize the imbalance in the flow following previous studies of gravity wave activity at Chatanika (Triplett et al., 2017).

The Sounding of the Atmosphere using Broadband Emission Radiometry (SABER) is one of four instruments aboard the Thermosphere-Ionosphere-Mesosphere Energetics and Dynamics satellite that was launched on 7 December 2001. SABER uses the technique of limb-infrared radiometry and is capable of continuously sounding the atmosphere both day and night. The SABER pressure data yield measurements of geopotential suitable for quantitative studies of the large-scale variability in the middle atmosphere (Byrd, 2016; Remsberg et al., 2008). We use the Level 2A version 2.0 SABER geopotential and temperature measurements and established procedures to determine planetary wave amplitudes, and gradient winds to characterize the planetary wave activity (Irving et al., 2014; Thurairajah, Collins, Harvey, Lieberman, & Mizutani, 2010; Thurairajah, Collins, Harvey, Lieberman, Gerding, et al., 2010).

The MSIS model is an analytical model for calculating neutral temperature and density profiles from the ground to the thermosphere (Hedin, 1991; Papitashvili, 2016). The density and temperature profiles are representative of the climatological average. Above 73 km the model is based on satellite, rocket, space shuttle, and incoherent scatter radar measurements. Between 20 and 73 km the model is primarily based on the monthly mean climatology of the Middle Atmosphere Program (Labitzke et al., 1985). Below 20 km the model uses averages from the National Meteorological Center. We take the MSIS density profile as having a 10% uncertainty in the upper mesosphere and lower thermosphere (Moro et al., 2016).

3. Observations

3.1. Arctic Meteorology

A minor SSW occurred in early January 2015 (Manney et al., 2015). Planetary wave activity had contributed to the development of strong anticyclones in the upper stratosphere in mid-December and early January and resulted in the subsequent splitting of the stratospheric vortex in the lower stratosphere on 1 January and throughout the stratosphere by 5 January. Although this SSW was classified as minor (during which the 10-hPa winds remained westerly at 60°N), the warming resulted in significant impacts on transport and chemical processing inside the polar vortex. The vortex reformed by 9 January and remained offset from the pole. On 26 January the polar vortex was located over Eurasia and Chatanika lay outside the edge of the vortex. The disturbance of the middle atmosphere is evident in the MERRA-2 winds over Chatanika plotted in Figure 5. We see that the winds through the middle and upper stratosphere weaken significantly in early January at at 10 and 1 hPa (~31 and ~48 km respectively) coinciding with the SSW. The MTeX investigation was conducted during a second weakening of the winds in late January. The wind profile at Chatanika on 5

January UT shows winds that are similar to the median winds for January, while the wind profile on 26 January UT shows winds that are considerably weaker than the median winds and are less than 15 m/s between 100 and 1 hPa (~16 and ~48 km respectively).

The SABER measurements also confirm this picture of a disturbed middle atmosphere. There was a reversal of the gradient winds at 65°N in early January associated with the SSW. We plot the planetary wave activity and winds derived from the SABER measurements for 26 January UT in Figure 6. The upper panel shows the geopotential height perturbation as a function of longitude and altitude. The data reveal a relatively weak planetary wave-1 that was propagating westward with altitude. The regions where the phase of the wave changed abruptly in altitude with coincident temperature inversions indicate planetary wave breaking (e.g., 55 km, 210°–270°E; France et al., 2015; Irving et al., 2014; Salby et al., 2002). These phase changes are also evident in the lower panel, where we plot the geopotential height perturbation as a function of altitude and latitude. Again, we see that the positive phase of the planetary wave reversed abruptly near 50 km, rather than propagating upward, indicating wave breaking in the upper stratosphere. The gradient winds derived from the SABER on this day show zonally averaged wind speeds that are low throughout the stratosphere and mesosphere over Chatanika consistent with MERRA-2 winds.

We characterize the balance in the circulation using the reanalysis data. The residual of the nonlinear balance equation has low values in the middle atmosphere that remain lower than the threshold for gravity wave generation (Limpasuvan et al., 2011; Triplett et al., 2017). Thus, we conclude that in January 2015, the middle atmosphere was disturbed, with weak winds at the end of the month, planetary wave breaking, and low levels of imbalance in the circulation.

3.2. Geomagnetic Activity

The aurora was moderately active on the night of 25–26 January 2015. The planetary *K* index was less than five, being three throughout most of the night and reaching four from 0000 to 0300 LST (0900–1200 UT; Matzka & Stolle, 2017; Vancanneyt & de Bont, 2017). By 1800 LST (0300 UT), the ASI recorded an active auroral arc near the northern horizon. A substorm breakup had been initiated to the east followed by a westward traveling surge that covered the sky by 0830 UT. Bright auroral arcs overhead were present until 0100 LST (1000 UT). These arcs had magenta lower borders indicating that the auroral precipitation was ionizing the atmosphere down to 90 km (e.g., Lummerzheim & Lilensten, 1994). The auroral display then weakened, but there was diffuse aurora overhead into the morning. The magnetometer recorded negative excursions in the horizontal component of the magnetic field starting at 2300 LST (0800 UT). The magnetic field excursion remained negative until 0140 LST (1040 UT) with a maximum excursion of ~400 nT at 0105 LST (1005 UT) and several fluctuations of ~100 nT. At the time of the MTeX launches there was bright aurora overhead with auroral arcs passing from north to south and negative excursions in the horizontal magnetic field of ~400 nT. The MTeX launches occurred after breakup in the recovery phase of the auroral substorm. We plot the electron density profiles and relative electron density gradients in Figure 7. The density profile measured by the Langmuir Probes

are in good agreement with the profile measured by PFISR. The electron densities are over 10^{11} m^{-3} above 100 km consistent with the auroral precipitation. The strongest gradients in the electron densities are near 80 and 90 km. These gradients are consistent with the auroral precipitation and the presence of arcs with magenta lower borders. However, despite the active auroral display, PFISR measured relatively weak electric fields. Thus, we conclude that the moderate geomagnetic activity did not significantly impact the neutral dynamics of the upper mesosphere and lower thermosphere.

3.3. Temperatures at Chatanika

The temperature profile over Chatanika on the night of 25–26 January 2015 reflects the disturbance of the atmosphere due to the stratospheric planetary wave activity. The temperature profiles do not show a well-defined stratopause. We plot the temperature profiles measured by the Rayleigh lidar in Figure 8. In the left panel we plot the temperature as a function of altitude and time based on 2-hr temperature profiles. In the center panel we plot the nightly average temperature profile (1827–0714 LST, 0327–1614 UT) and the 2-hr temperature profile around the launch of the MTeX payloads (2315–0115 LST, 0830–1030 UT). We also plot the average temperature profile for January based on 35 nighttime observations made between 1998 and 2014 (Triplett et al., 2017). On the night of 25–26 January 2015 the stratosphere is colder than the average (by about one sample standard deviation) and the mesosphere is warmer than the average (by about two sample standard deviations). In the right panel we plot the nightly average and 2-hr temperature profiles over the 75- to 95-km altitude range. The nightly average maximum temperature is 238 K at 67 km, and there is well-defined temperature gradient of –4 K/km above 85 km that persisted through the night. The 2-hr temperature profile shows a MIL present at 85 km. This MIL has an amplitude of 13 K with an overlying super-adiabatic temperature gradient of –18 K/km. This inversion layer is present over a 4-hr period from 2130 to 0130 LST (0630–1030 UT) between 83 and 86 km with an average peak altitude of 84 km, depth of 1.4 km, amplitude of 9 K, and average topside temperature gradient of –12 K/km.

We plot the three temperature profiles derived from the CONE measurements in Figure 9. All three CONE profiles have similar features with a MIL near 80 km and a negative temperature gradient above the MIL extending upward from an altitude between 83 and 85 km. The amplitude of this MIL is between 9 and 14 K with a topside temperature gradient between –6 and –10 K/km. Another MIL is present near 74 km in both the upleg and downleg of 46.009. This MIL has an amplitude between 11 and 16 K and a topside temperature gradient of –6 K/km. The negative temperature gradient above 85 km is consistent with SABER multiyear measurements of the Arctic winter mesopause at 100 km (Xu et al., 2007).

In summary the Rayleigh lidar and CONE temperature measurements show a disturbed stratosphere and mesosphere where there are MILs present. There are multiple altitude regions with negative temperature gradients in the upper mesosphere, and several of these regions are convectively unstable.

3.4. Gravity Waves at Chatanika

We first determine the wave activity over the 40- to 50-km altitude range consistent with previous studies of gravity wave activity at Chatanika that includes waves with vertical wavelengths between 2 and 10 km (Table 2). We find a specific potential energy of 0.8 J/kg. This level of gravity wave activity is among the lowest values measured by Rayleigh lidar at Chatanika (Triplett et al., 2017). In 35 nighttime measurements in January over 13 winters at Chatanika the specific potential energies of gravity waves vary between 0.4 and 12 J/kg with an average value of 2.6 J/kg and only three values less than 0.8 J/kg. Low levels of gravity wave activity have been shown to be consistent with weak winds and low levels of imbalance in the circulation (Triplett et al., 2017). To understand the vertical propagation of gravity waves, we determine the gravity wave activity over two distinct altitude ranges. We consider the gravity wave activity over a lower range of 37.5 to 52.5 km and an upper range of 62 to 77 km that includes waves with vertical wavelengths between 2 and 15 km. We summarize the wave characteristics in Table 2. In the lower range we find a specific potential energy of 1.7 J/kg. In the upper range we find a specific potential energy of 6.4 J/kg. The specific potential energy increases by a factor of 3.8 corresponding to a growth length of 18 km. The density scale height over this altitude range is 7 km indicating that the specific potential energy of freely propagating gravity waves would increase by a factor of 33. We conclude that these gravity waves are losing energy as they propagate upward.

We find two monochromatic waves in the Rayleigh lidar density profiles. We find a 9.8-hr wave present in both the stratosphere (44 to 51 km) and mesosphere (63 to 73 km). This wave exhibits a downward phase progression consistent with a vertical wavelength of 8 km (±4 km) in the stratosphere and 12 km (±7 km) in the mesosphere. The amplitude of the wave is 0.73% in the stratosphere and 1.3% in the mesosphere. We also find a 2.5-hr wave present in the stratosphere (41 to 50 km) and mesosphere (64 to 77 km). This 2.5-hr wave is only present during the first half of the night until 0000 LST (0900 UT) in the mesosphere. The vertical wavelength of the 2.5-hr wave is 11 km (±5 km) in the stratosphere and 6 km (±4 km) in the mesosphere. The amplitude of the wave is 0.36% in the stratosphere and 1.2% in the mesosphere. We summarize the characteristics of these waves in Table 3. The derived quantities are determined from the measured quantities using gravity wave dispersion and polarization relationships (Hines, 1960). The growth lengths of the 9.8- and 2.5-hr waves are 18 and 10 km, respectively, indicating that the waves are losing energy as they propagate upward. The horizontal phase speeds are greater than the RMS horizontal velocities indicating that the individual waves are linearly stable at these altitudes (Fritts & Rastogi, 1985). However, the waves grow with altitude and by 76 km the combined RMS horizontal velocity of both waves is greater than the horizontal phase speed of the 2.5-hr wave. Thus, the shorter-period 2.5-hr wave may be rendered unstable by the superposition of the longer-period wave and the shorter-period wave as has been documented in other observational studies (Collins & Smith, 2004; Fritts et al., 1997; Williams et al., 2006).

3.5. Turbulence at Chatanika

The CONE measurements yielded 140 estimates of turbulence between 70 and 88 km. The RMS relative density fluctuations vary between 0.02% and 0.39% with an average value of 0.1%. Over the 70- to 88-km altitude region the turbulent inner scales vary between 12 and

121 m with an average value of 56 m. The energy dissipation rates vary between 0.1 and 24 mW/kg with an average value of 2.6 mW/kg. We plot the estimates of the energy dissipation rate and the turbulent inner scale with the temperature profiles measured by the CONE instrument in Figure 10. The corresponding heating rates vary between 9×10^{-3} K/day and 2 K/day with an average of 0.2 K/day. The corresponding eddy diffusion rates vary between 0.3 m^2/s and 134 m^2/s with an average of 10 m^2/s. The individual turbulent estimates plotted in Figure 10 are not mutually independent as they represent estimates over overlapping 1 s (~1 km) intervals. However, the turbulence occurs in clusters that extend over 1 km in altitude. There are eight clusters in the both the upleg and downleg of 46.009, and there are three clusters in the downleg of 46.010. The absence of turbulence at the lower altitudes in the downleg of 46.010 (lower panel) coincides with the absence of a MIL. Of the 19 turbulence clusters, four coincide with a MIL bottomside, nine coincide with a MIL topside, and six coincide with the negative temperature gradient above the MILs at altitudes above 84 km. To investigate the relationship between turbulence and stability, we consider the relationship between the energy dissipation rate and the square of the buoyancy frequency. In each cluster we identify the maximum estimate of the energy dissipation rate and the corresponding buoyancy frequency. We also determine the location of the turbulence relative to the MILs (i.e., topside or bottomside) and the temperature profile above the MILs (i.e., temperature gradient). We plot these maximum energy dissipation rates as a function of buoyancy frequency squared in Figure 11. While the largest values of energy dissipation rates coincide with the negative temperature gradient at the highest altitudes (0.8–24 mW/kg), the values of the turbulent dissipation rate are similar on both the topside (0.3–11 mW/kg) and bottomside (0.4–7 mW/kg) of the MILs, with no significant difference in the average values. The corresponding values of the eddy diffusion coefficient increase as the buoyancy frequency decreases, and the values are larger in the topside of the MILs (1–134 m^2/s) and the negative temperature gradient (4–54 m^2/s) than in the bottomside of the MILs (0.4–11 m^2/s).

In general, the MTeX measurements show turbulence occurring in two distinct altitude regions with lower values of energy dissipation at lower altitudes (70–77 km) and higher values at higher altitudes (79–88 km). We summarize the turbulence characteristics in Table 4. We find that the inner scale increases with altitude from 26 to 70 m and the corresponding outer scales increase from 129 m to 360 m. The turbulent dissipation rate also increases, by a factor of 3, from 1 to 3 mW/kg over 10 km. These dissipation rates correspond to heating rates of 0.1 and 0.3 K/day.

4. Analysis of Turbulence and Waves

4.1. Waves as a Source of Turbulence

To understand these low levels of turbulence, we consider the gravity waves we identified in section 3.4 as sources of the turbulence. We plot the sodium concentration as a function of altitude and time in the upper panel of Figure 12. The sodium has downward phase progressions typical of wave propagation through the sodium layer and overturning between 80 and 90 km between 2200 LST and 0230 LST (0700–1130 UT). Model studies of such overturning events indicate that these are signatures of waves that are approaching instability

(Xu et al., 2006). We also plot the potential temperature and sodium mixing ratio in the lower panel of Figure 12. The potential temperature contours spread apart with a near vertical contour at 2230 LST at the same time as the overturning in the sodium concentration. During this overturning event the sodium mixing ratio also spreads upward. The spreading of the potential temperature and sodium extends over a depth of 3 km in altitude and persists for 2 hr in time. The upward spreading of the 600-K potential temperature contour is consistent with numerical studies of wave breaking where a layer of cooling due to wave advection overlies a layer of heating due to turbulent diffusion (Liu et al., 2000). High-resolution lidar observations of sodium and temperature have shown that such overturning events are associated with spreading of energy to higher frequencies in the temporal temperature spectrum and generation of smaller-scale motions (Franke & Collins, 2003; Williams et al., 2002).

We use the depth of the wave breaking to estimate the energy that can be deposited by the gravity waves and available for the generation of turbulence. We assume that as the wave dissipates, all the energy that is lost generates inertial subrange turbulence. However, in reality the dissipating waves will generate a variety of other motions (e.g., secondary waves) as well as turbulence (VanZandt & Fritts, 1989). We consider a breaking altitude of 85 km coincident with the spreading of the 20-pptv mixing ratio contour in Figure 12. We first consider the 2.5-hr wave. We allow the 2.5-hr wave to grow with an energy growth length of 10 km from 70 to 85 km. The wave has a vertical group velocity of 2.5 km/hr and would deposit all of its potential energy over 3 km in 1.2 hr, yielding an energy dissipation rate of 18 mW/kg. We second consider the ensemble of 1- to 4-hr waves. For this ensemble of waves, with a geometric mean period of 2 hr and a vertical wavelength of 5.5 km, the corresponding vertical group velocity is 2.7 km/hr. We allow the waves to grow with an energy growth length of 18 km from 65 to 85 km and determine the energy lost relative to waves that are freely propagating with a growth length of 7 km. The energy lost is 92 J/kg in 7.7 hr yielding an energy dissipation rate of 3 mW/kg. We find that the relatively low levels of turbulent energy dissipation are consistent with the low level of gravity wave energy.

4.2. Strength of Turbulence

We compare the MTeX measurements of turbulence to other Arctic measurements. We consider three studies based on Arctic rocket-borne ion gauges (Lübken, 1997 [L97]; Lehmacher et al., 2011 [Letal11], and Szewczyk et al., 2013 [Setal13]). We plot the energy dissipation rates and eddy diffusion coefficients from MTeX and these three investigations in Figure 13. It is important to note that for MTeX, Letal11, and Setal13, the ion gauges made measurements above the maximum altitudes plotted (i.e., 88 km MTeX, 90 km Letal11, 93 km Setal13) but did not detect turbulence. We conclude that there was no detectible turbulence present above these altitudes. The Letal11 and Setal13 profiles were measured on single nights at Chatanika on 17–18 February 2009 and at Andennes on 18–19 December 2010, respectively. The L97-W profile represents the average of 12 wintertime measurements over two winters at Andøya Science Center, Andennes, Norway (69°N, 16°E). The L97-S profile represents the average of seven summertime measurements over three summers at Andennes. The MTeX values of turbulent activity increase with altitude, but the peak values are similar to the peak values from Letal11 and much lower than the

peak values from Setal13. The MTeX average values are lower than the L97-W values. The turbulent energy dissipation rates in winter (L97-W) are 10 times less than in summer (L97-S) and have been interpreted to indicate low levels of turbulent dissipation and heating in the wintertime Arctic middle atmosphere. The transition from wintertime to summertime turbulence values has been observed and attributed to seasonal transitions in the breaking of gravity waves associated with changes in the wind regimes (Müllemann et al., 2002).

Both the low values of turbulent activity reported by MTeX and Letal11 are similar to the low values of wintertime turbulence reported by L97. The Letal11 turbulence measurements at Chatanika were accompanied by Rayleigh lidar measurements of the temperature profile and gravity wave activity. The meteorological conditions at Chatanika in both January 2015 and February 2009 are similar. In 2009 there was a major SSW in late January and the middle atmosphere remained disturbed until March (Manney et al., 2009). The Rayleigh lidar temperature profile at Chatanika on the night of 17–18 February 2009 shows a stratosphere that is colder than usual and a mesosphere that is warmer than usual similar to MTeX (Collins et al., 2011). We plot the MERRA-2 wind profiles in Figure 14. The wind profiles on the night of 17–18 February 2009 (18 February UT) show horizontal wind speeds at Chatanika of less than 15 m/s between 100 and 2 hPa (~16 km and ~43 km respectively) similar to MTeX. On both nights the winds are significantly lower than the median winds for January and February at Chatanika. On 17–18 February 2009, like on 25–26 January 2015, the gravity wave activity in the 40- to 50-km region was low with a specific potential energy of 0.9 J/kg. MTeX and Letal11 report a consistent scenario of low turbulent activity associated with reduced gravity wave activity during a period when the circulation of the stratosphere and mesosphere is disturbed and the winds are weak. Observational studies at Chatanika have shown that weak winds (<15 m/s) in the lower stratosphere block the upward propagation of gravity waves and reduce the gravity wave activity in the lower mesosphere (Thurairajah, Collins, Harvey, Lieberman, & Mizutani, 2010; Thurairajah, Collins, Harvey, Lieberman, Gerding, et al., 2010; Triplett et al., 2017).

In contrast to MTeX and Letal11 the values of turbulence reported by Setal13 are significantly higher. Setal13 report significant wave activity in the upper mesosphere but do not report the stratospheric wave activity. The MERRA-2 wind profiles on the night of 18–19 December 2010 show horizontal wind speeds at Andennes that increase steadily between 100 and 2 hPa (~16 km and ~43 km respectively) to 48 m/s. There was no SSW during the winter of 2010–2011, and the circulation was undisturbed with an unusually strong polar vortex and unprecedented ozone loss in March 2011 (Manney et al., 2011). The higher turbulent activity reported by Setal13 was recorded during a period when the circulation of the stratosphere and mesosphere was undisturbed, winds were strong, and the gravity wave activity was high.

5. Summary and Conclusions

We have presented a study of turbulence in the upper mesosphere-lower thermosphere following a minor SSW in January 2015 where the circulation remained disturbed due to continued planetary wave activity. The study, called MTeX, combined in situ rocket-borne measurements of turbulence with ground-based lidar measurements of gravity wave activity,

satellite measurements of planetary wave activity, and reanalysis data of the meteorological conditions. The circulation was characterized by weak winds and the absence of a distinct stratopause. We find low levels of turbulence coinciding with reduced levels of gravity wave activity. The average turbulent energy dissipation rate was 2.6 mW/kg, and the average eddy diffusion coefficient was 10 m^2/s. This average energy dissipation rate corresponds to a heating rate of 0.2 K/day. The turbulence was detected in an altitude region where there were MILs and overturning gravity waves. The turbulence is found on both the bottomside and topside of the MILs as well as regions of negative temperature gradients. The wave overturning event is characterized by upward altitude spreading in both potential temperature and sodium mixing ratio. Investigation of the propagation of the energy in both the ensemble gravity wave field and monochromatic gravity waves confirms that the low levels of turbulence coincide with the low levels of gravity wave activity. The MTeX measurements reveal the occurrence of low levels of turbulence and wave activity in a disturbed winter middle atmosphere where weak winds block the upward propagation of gravity waves. Higher planetary wave activity in the northern hemisphere than the southern hemisphere results in much greater disturbance of the circulation of the Arctic middle atmosphere. We suggest that there may be lower levels of wave-driven turbulence in the wintertime northern hemisphere than in the southern hemisphere. This scenario has been suggested in an earlier model study where the weaker and more variable polar night jet in the northern hemisphere results in gravity wave breaking over a greater depth and lower altitude and significant decrease in turbulent diffusion in the MLT than in the southern hemisphere (Becker, 2004).

The MTeX investigation was based on high-resolution density measurements and derived temperature measurements made with ion gauges and lidars. The wave observations are limited to inertia gravity waves with periods of more than 1 hr and vertical wavelengths greater than 2 km. The wave scales and turbulent scales measured during MTeX are separated by an order of magnitude. A sodium resonance wind-temperature lidar is currently being deployed at PFRR and will provide measurements of higher frequency gravity waves. A meteor radar system is currently being deployed at PFRR and will be able to provide wind measurements and characterization of waves and tides in support of future investigations.

Supplementary Material

Refer to Web version on PubMed Central for supplementary material.

Acknowledgments

References

Becker E (2004). Direct heating rates associated with gravity wave saturation. Journal of Atmospheric and Solar - Terrestrial Physics, 66(6–9), 683–696. 10.1016/j.jastp.2004.01.019

Becker E (2012). Dynamical control of the middle atmosphere. Space Science Reviews, 168(1–4), 283–314. 10.1007/s11214-011-9841-5

Bishop RL, Larsen MF, Hecht JH, Liu AZ, & Gardner CS (2004). TOMEX: Mesospheric and lower thermospheric diffusivities and instability layers. Journal of Geophysical Research, 109, D02S03 10.1029/2002JD003079

Blake A (2014). Langmuir probe instrument suite for mesosphere turbulence experiment mission (MS Thesis), (153 pp.), Embry Riddle Aeronautical University.

Blix TA, Thrane EV, & Andreassen Ø (1990). In situ measurements of the fine-scale structure and turbulence in the mesosphere and lower thermosphere by means of electrostatic positive ion probes. Journal of Geophysical Research, 95(D5), 5533–5548. 10.1029/JD095iD05p05533

Bosilovich MG, Akella S, Coy L, Cullather R, Draper C, Gelaro R, et al. (2015), MERRA2: Initial evaluation of the climate, NASA Tech. Rep. Series on Global Modeling and Data Assimilation, NASA/TM–2015–104606, Vol. 43.

Byrd TG (2016). SABER—Sounding of the Atmosphere using Broadband Emission Radiometry http://saber.gats-usa.net/data.php, GATS, Newport News, VA.

Collins R, Triplett C, Barjatya A, Lehmacher G, & Fritts D (2015). Using lidar and rockets to explore turbulence in the atmosphere. SPIE Newsroom 10.1117/2.1201505.005922

Collins RL, Hallinan TJ, Smith RW, & Hernandez G (1996). Lidar observations of a large high-altitude sporadic Na layer during active aurora. Geophysical Research Letters, 23(24), 1944–8007. 10.1029/96GL03337

Collins RL, Lehmacher GA, Larsen MF, & Mizutani K (2011). Estimates of vertical eddy diffusivity in the upper mesosphere in the presence of a mesospheric inversion layer. Annales de Geophysique, 29(11), 2019–2029. 10.5194/angeo-29-2019-2011

Collins RL, & Smith RW (2004). Evidence of damping and overturning of gravity waves in the arctic mesosphere: Na lidar and OH temperature observations. Journal of Atmospheric and Solar - Terrestrial Physics, 66(10), 867–879. 10.1016/j.jastp.2004.01.038

Dutton JA (1988). The ceaseless wind: An introduction to the theory of atmospheric motion (p. 617). New York: Dover Publications, Inc.

France JA, Harvey VL, Randall CE, Collins RL, Smith AK, Peck ED, & Fang X (2015). A climatology of planetary wave-driven mesospheric inversion layers in the extratropical winter. Journal of Geophysical Research: Atmospheres, 120, 399–413. 10.1002/2014JD022244

Franke PM, & Collins RL (2003). Evidence of gravity wave breaking in lidar data from the mesopause region. Geophysical Research Letters, 30(4), 1155 10.1029/2001GL014477

Fritts DC, & Alexander MJ (2003). Gravity wave dynamics and effects in the middle atmosphere. Reviews of Geophysics, 41(1), 1003 10.1029/2001RG000106

Fritts DC, Isler JR, Hecht JH, Walterscheid RL, & Andreassen Ø (1997). Wave breaking signatures in sodium densities and OH nightglow: 2. Simulation of wave and instability structures. Journal of Geophysical Research, 102(D6), 6669–6684. 10.1029/96JD01902

Fritts DC, Laughman B, Wang L, Lund TS, & Collins RL (2018). Gravity wave dynamics in a mesospheric inversion layer: 1. Reflection, trapping, and instability dynamics. Journal of Geophysical Research: Atmospheres, 123(2), 626–648. 10.1002/2017JD027440

Fritts DC, & Rastogi PK (1985). Convective and dynamical instabilities due to gravity wave motions in the lower and middle atmosphere: Theory and observations. Radio Science, 20(6), 1247–1277. 10.1029/RS020i006p01247

Fritts DC, Wang L, Baumgarten G, Miller AD, Geller MA, Jones G, et al. (2017). High-resolution observations and modeling of turbulence sources, structures, and intensities in the upper mesosphere. Journal of Atmospheric and Solar - Terrestrial Physics, 162, 57–78. 10.1016/j.jastp. 2016.11.006

Fujiwara M, Wright JS, Manney GL, Gray LJ, Anstey J, Birner T, et al. (2017). Introduction to the SPARC Reanalysis Intercomparison Project (S-RIP) and overview of the reanalysis systems. Atmospheric Chemistry and Physics, 17(2), 1417–1452. 10.5194/acp-17-1417-2017

Garcia RR, López-Puertas M, Funke B, Marsh DR, Kinnison DE, Smith AK, & González-Galindo F (2014). On the distribution of CO_2 and CO in the mesosphere and lower thermosphere. Journal of Geophysical Research: Atmospheres, 119, 5700–5718. 10.1002/2013JD021208

Gass J (2016), Modern-Era Retrospective analysis for Research and Applications, Version 2 https://gmao.gsfc.nasa.gov/reanalysis/MERRA2/, NASA Goddard Space Flight Center.

Gelaro R, McCarty W, Suárez MJ, Todling R, Molod A, Takacs L, et al. (2017). The Modern-Era Retrospective Analysis for Research and Applications, Version 2 (MERRA-2). Journal of Climate, 30(14), 5419–5454. 10.1175/JCLI-D-16-0758.1

Gelinas LJ, Lynch KA, Kelley MC, Collins RL, Widholm M, MacDonald E, et al. (2005). Mesospheric charged dust layer: Implications for neutral chemistry. Journal of Geophysical Research, 110, A01310 10.1029/2004JA010503

Giebeler J, Lübken F-J, and Nägele M (1993), CONE—A new sensor for in situ observations of neutral and plasma density fluctuations. Proc. 11th ESA Symp. Europ. Rocket Balloon Progr, Montreux, Switzerland, ESA SP-355, 311–318.

Grygalashvyly M, Becker E, & Sonnemann GR (2011). Wave mixing effects on minor chemical constituents in the MLT region: Results from a global CTM driven by high-resolution dynamics. Journal of Geophysical Research, 116, D18302 10.1029/2010JD015518

Guo Y, Liu AZ, & Gardner CS (2017). First Na lidar measurements of turbulence heat flux, thermal diffusivity, and energy dissipation rate in the mesopause region. Geophysical Research Letters, 44, 5782–5790. 10.1002/2017GL073807

Hampton DL (2017a). Archived Poker three-filter all-sky movies http://optics.gi.alaska.edu/realtime/data/MPEG/PKR_DASC_256/, Geophysical Institute, University of Alaska Fairbanks.

Hampton DL (2017b). Geophysical Institute Magnetometer Array http://magnet.gi.alaska.edu, Research Computing Systems, Geophysical Institute, University of Alaska Fairbanks.

Hedin AE (1991). Extension of the MSIS thermosphere model into the middle and lower atmosphere. Journal of Geophysical Research, 96(A2), 1159–1172. 10.1029/90JA02125

Heinselman CJ, & Nicolls MJ (2008). A Bayesian approach to electric field and E-region neutral wind estimation with the Poker Flat Advanced Modular Incoherent Scatter Radar. Radio Science, 43, RS5013 10.1029/2007RS003805

Hines CO (1960). Internal gravity waves at ionospheric heights. Canadian Journal of Physics, 38(11), 1441–1481. 10.1139/p60-150

Hines CO (1988). Generation of turbulence by atmospheric gravity waves. Journal of the Atmospheric Sciences, 45(7), 1269–1278. 10.1175/1520-0469(1988)045<1269:GOTBAG>2.0.CO;2

Irving BK, Collins RL, Lieberman RS, Thurairajah B, & Mizutani K (2014). Mesospheric inversion layers at Chatanika, Alaska (65°N, 147°W): Rayleigh lidar observations and analysis. Journal of Geophysical Research: Atmospheres, 119, 11,235–11,249. 10.1002/2014JD021838

Labitzke K, Barnett JJ, & Edwards B (Eds.) (1985). Atmospheric structure and its variation in the region 20 to 120 km: Draft of a new reference middle atmosphere. Handbook for MAP, 16, SCOSTEP, University of Illinois, Urbana, USA.

Lehmacher GA, Croskey CL, Mitchell JD, Friedrich M, Lübken F-J, Rapp M, et al. (2006). Intense turbulence observed above a mesospheric temperature inversion at equatorial latitude. Geophysical Research Letters, 33, L08808 10.1029/2005GL024345

Lehmacher GA, & Lübken F-J (1995). Simultaneous observation of convective adjustment and turbulence generation in the mesosphere. Geophysical Research Letters, 22(18), 2477–2480. 10.1029/95GL02351

Lehmacher GA, Scott TD, Larsen MF, Bilén S, Croskey CL, Mitchell JD, et al. (2011). The Turbopause experiment: Atmospheric stability and turbulent structure spanning the turbopause altitude. Annales de Geophysique, 29(12), 2327–2339. 10.5194/angeo-29-2327-2011

Limpasuvan V, Alexander MJ, Orsolini YJ, Wu DL, Richter JH, & Yamashita C (2011). Mesoscale simulation of gravity waves during the 2008–2009 major stratospheric sudden warming. Journal of Geophysical Research, 116, D17104 10.1029/2010JD015190

Liu H-L, Hagan ME, & Roble RG (2000). Local mean state changes due to gravity wave breaking modulated by the diurnal tide. Journal of Geophysical Research, 105(D10), 12,381–12,396. 10.1029/1999JD901163

Liu H-L, & Meriwether JW (2004). Analysis of a temperature inversion event in the lower mesosphere. Journal of Geophysical Research, 109, D02S07 10.1029/2002JD003026

López-Puertas M, Funke B, von Clarmann T, Fischer H, & Stiller GP (2006). The stratospheric and mesospheric NOy in the 2002–2004 polar winters as measured by MIPAS/ENVISAT. Space Science Reviews, 125(1–4), 403–416. 10.1007/s11214-006-9073-2

Lübken F-J (1992). On the extraction of turbulent parameters from atmospheric density fluctuations. Journal of Geophysical Research, 97(D18), 20,385–20,395. 10.1029/92JD01916

Lübken F-J (1997). Seasonal variation of turbulent energy dissipation rates at high latitudes as determined by in situ measurements of neutral density fluctuations. Journal of Geophysical Research, 102(D12), 13,441–13,456. 10.1029/97JD00853

Lübken F-J, Hillert W, Lehmacher GA, & von Zahn U (1993). Experiments revealing small impact of turbulence on the energy budget of the mesosphere and lower thermosphere. Journal of Geophysical Research, 98(D11), 20,369–20,384. 10.1029/93JD02055 [PubMed: 11539182]

Lübken F-J, Rapp M, & Hoffmann P (2002). Neutral air turbulence and temperatures in the vicinity of polar mesosphere summer echoes. Journal of Geophysical Research, 107(D15), 4273 10.1029/2001JD000915

Lummerzheim D, & Lilensten J (1994). Electron transport and energy degradation in the ionosphere: Evaluation of the numerical solution, comparison with laboratory experiments and auroral observations. Annales de Geophysique, 12(10/11), 1039–1051. 10.1007/s00585-994-1039-7

Lyons LR, Nishimura Y, Gallardo-Lacourt B, Nicolls MJ, Chen S, Hampton DL, et al. (2015). Azimuthal flow bursts in the inner plasma sheet and possible connection with SAPS and plasma sheet earthward flow bursts. Journal of Geophysical Research: Space Physics, 120, 5009–5021. 10.1002/2015JA021023

Manney GL, Lawrence ZD, Santee ML, Read WG, Livesey NJ, Lambert A, et al. (2015). A minor sudden stratospheric warming with a major impact: Transport and polar processing in the 2014/2015 Arctic winter. Geophysical Research Letters, 42, 7808–7816. 10.1002/2015GL065864.

Manney GL, Santee ML, Rex M, Livesey NJ, Pitts MC, Veefkind P, et al. (2011). Unprecedented Arctic ozone loss in 2011. Nature, 478(7370), 469–475. 10.1038/nature10556 [PubMed: 21964337]

Manney GL, Schwartz MJ, Krüger K, Santee ML, Pawson S, Lee JN, et al. (2009). Aura Microwave Limb Sounder observations of dynamics and transport during the record-breaking 2009 Arctic stratospheric major warming. Geophysical Research Letters, 36, L12815 10.1029/2009GL038586

Martus CM (2013). Exploration of mesospheric metal layers from Chatanika, Alaska, (MS Thesis). (194 pp.). University of Alaska Fairbanks

Matzka J, and Stolle C (2017), Kp index archive GFZ German Research Center for Geosciences, Helmholtz Center, Potsdam https://www.gfz-potsdam.de/en/kp-index/.

Meraner K, & Schmidt H (2016). Transport of nitrogen oxides through the winter mesopause in HAMMONIA. Journal of Geophysical Research: Atmospheres, 121, 2556–2570. 10.1002/2015JD024136

Meriwether JW, & Gerrard AJ (2004). Mesosphere inversion layers and stratosphere temperature enhancements. Reviews of Geophysics, 42, RG3003 10.1029/2003rg000133

Mironova IA, Aplin KL, Arnold F, Bazilevskaya GA, Harrison RG, Krivolutsk AA, et al. (2015). Energetic particle influence on the Earth's atmosphere. Space Science Reviews, 194(1–4), 1–96. 10.1007/s11214-015-0185-4

Molod A, Takacs L, Suarez M, & Bacmeister J (2015). Development of the GEOS-5 atmospheric general circulation model: Evolution from MERRA to MERRA2. Geoscientific Model Development, 8(5), 1339–1356. 10.5194/gmd-8-1339-2015

Moro J, Denardini CM, Resende LCA, Chen SS, & Schuch NJ (2016). Influence of uncertainties of the empirical models for inferring the E-region electric fields at the dip equator. Earth, Planets and Space, 68(1). 10.1186/s40623-016-0479-0

Müllemann A, Rapp M, Lubken F, & Hoffmann P (2002). In situ measurements of mesospheric turbulence during spring transition of the Arctic mesosphere. Geophysical Research Letters, 29(10), 1477 10.1029/2002GL014841

Papitashvili N (2016). Virtual Ionosphere, Thermosphere, Mesosphere Observatory (VITMO) MSIS-E-90 atmosphere model https://cohoweb.gsfc.nasa.gov/vitmo/msis_vitmo.html. NASA Goddard Space Flight Center.

Plougonven R, & Zhang F (2014). Internal gravity waves from atmospheric jets and fronts. Reviews of Geophysics, 52, 33–76. 10.1002/2012RG000419

Randall CE, Harvey VL, Singleton CS, Bernath PF, Boone CD, & Kozyra JU (2006). Enhanced NOx in 2006 linked to strong upper stratospheric Arctic vortex. Geophysical Research Letters, 33, L18811 10.1029/2006GL027160

Randall CE, Harvey VL, Siskind DE, France J, Bernath PF, Boone CD, & Walker KA (2009). NOx descent in the Arctic middle atmosphere in early 2009. Geophysical Research Letters, 36, L18811 10.1029/2009GL039706

Rapp M, Gumbel J, & Lübken F-J (2001). Absolute density measurements in the middle atmosphere. Annales de Geophysique, 19(5), 571–580. 10.5194/angeo-19-571-2001

Remsberg EE, Marshall BT, García-Comas M, Krueger D, Lingenfelser GS, Martin-Torres J, et al. (2008). Assessment of the quality of the version 1.07 temperature-versus-pressure profiles of the middle atmosphere from TIMED/SABER. Journal of Geophysical Research, 113, D17101 10.1029/2008JD010013

Salby M, Sassi F, Callaghan P, Wu D, Keckhut P, & Hauchecorne A (2002). Mesospheric inversions and their relationship to planetary wave structure. Journal of Geophysical Research, 107(D4), 4041 10.1029/2001JD000756

Sassi F, Garcia RR, Boville BA, & Liu H (2002). On temperature inversions and the mesospheric surf zone. Journal of Geophysical Research, 107(D19), 4380 10.1029/2001jd001525

Smith AK (2012). Global dynamics of the MLT. Surveys in Geophysics, 33(6), 1177–1230. 10.1007/s10712-012-9196-9

Smith AK, Garcia RR, Marsh DR, & Richter JH (2011). WACCM simulations of the mean circulation and trace species transport in the winter mesosphere. Journal of Geophysical Research, 116, D20115 10.1029/2011JD016083

Steigies CT, & Barjatya A (2012). Contamination effects on fixed-bias Langmuir probes. The Review of Scientific Instruments, 83(11), 113502 10.1063/1.4764582 [PubMed: 23206057]

Strelnikov B, Szewczyk A, Strelnikova I, Latteck R, Baumgarten G, Lübken F-J, et al. (2017). Spatial and temporal variability in MLT turbulence inferred from in situ and ground-based observations during the WADIS-1 sounding rocket campaign. Annales de Geophysique, 35(3), 547–565. 10.5194/angeo-35-547-2017.

Sutherland BR (2010). Internal gravity waves (p. 394). Cambridge: Cambridge University Press 10.1017/CBO9780511780318

Swenson G, Yee Y, Vargas F, & Liu A (2018). Vertical diffusion transport of atomic oxygen in the mesopause region consistent with chemical losses and continuity: Global mean and inter-annual variability. Journal of Atmospheric and Solar-Terrestrial Physics, 178, 47–55. 10.1016/j.jastp.2018.05.014

Szewczyk A (2015), Mesospheric turbulence: The role in the creation of mesospheric inversion layers and statistical results 148 pp., PhD Dissertation, Univ. Rostock.

Szewczyk A, Strelnikov B, Rapp M, Strelnikova I, Baumgarten G, Kaifler N, et al. (2013). Simultaneous observations of a Mesospheric Inversion Layer and turbulence during the ECOMA-2010 rocket campaign. Annales de Geophysique, 31(5), 775–785. 10.5194/angeo-31-775-2013

Thomas L, Marsh A, Wareing D, Astin I, & Chandra H (1996). VHF echoes from the midlatitude mesosphere and the thermal structure observed by lidar. Journal of Geophysical Research, 101(D8), 12,867–12,877. 10.1029/96JD00218

Thurairajah B, Collins RL, Harvey VL, Lieberman RS, Gerding M, Mizutani K, & Livingston JM (2010). Gravity wave activity in the Arctic stratosphere and mesosphere during the 2007–2008 and 2008–2009 stratospheric sudden warming events. Journal of Geophysical Research, 115, D00N06 10.1029/2010JD014125

Thurairajah B, Collins RL, Harvey VL, Lieberman RS, & Mizutani K (2010). Rayleigh lidar observations of reduced gravity wave activity during the formation of an elevated stratopause in 2004 at Chatanika, Alaska (65°N, 147°W). Journal of Geophysical Research, 115, D13109 10.1029/2009JD013036

Triplett CC (2016), Rocket and lidar studies of waves and turbulence in the Arctic middle atmosphere, 172 pp, PhD Dissertation, Univ. of Alaska Fairbanks.

Triplett CC, Collins RL, Nielsen K, Harvey VL, & Mizutani K (2017). Role of wind filtering and unbalanced flow generation in middle atmosphere gravity wave activity at Chatanika Alaska. Atmosphere, 8(12), 27 10.3390/atmos8020027

Vancanneyt S, & de Bont M (2017). GFZ Potsdam official Kp-index https://www.spaceweatherlive.com/en/archive/.

VanZandt TE, & Fritts DC (1989). A theory of enhanced saturation of the gravity wave spectrum due to increases in atmospheric stability. Pure and Applied Geophysics, 130(2–3), 399–420. 10.1007/BF00874466.

Walterscheid RL (2001). Gravity wave transports and their effects on the large-scale circulation of the upper mesosphere and lower thermosphere. Advances in Space Research, 27(10), 1713–1721. 10.1016/S0273-1177(01)00298-8

Weinstock J (1978). Vertical turbulent diffusion in a stably stratified fluid. Journal of the Atmospheric Sciences, 35(6), 1022–1027. 10.1175/1520-0469(1978)035<1022:VTDIAS>2.0.CO;2

Whiteway JA, Carswell AI, & Ward WE (1995). Mesospheric temperature inversions with overlying nearly adiabatic lapse rate: An indication of a well-mixed turbulent layer. Geophysical Research Letters, 22(10), 1201–1204. 10.1029/95gl01109

Williams BP, Fritts DC, She CY, & Goldberg RA (2006). Gravity wave propagation through a large semidiurnal tide and instabilities in the mesosphere and lower thermosphere during the winter 2003 MaCWAVE rocket campaign. Annales de Geophysique, 24(4), 1199–1208. 10.5194/angeo-24-1199-2006

Williams BP, White MA, Krueger DA, & She CY (2002). Observation of a large amplitude wave and inversion layer leading to convective instability in the mesopause region over Fort Collins CO (41°N, 105°W). Geophysical Research Letters, 29(17), 1850 10.1029/2001GL014514

Xu J, Liu H-L, Yuan W, Smith AK, Roble RG, Mertens CJ, Russell JM III, et al. (2007). Mesopause structure from Thermosphere, Ionosphere, Mesosphere, Energetics, and Dynamics (TIMED)/Sounding of the Atmosphere Using Broadband Emission Radiometry (SABER) observations. Journal of Geophysical Research, 112, D09102 10.1029/2006JD007711

Xu J, Smith AK, Collins RL, & She C-Y (2006). Signature of an overturning gravity wave in the mesospheric sodium layer: Comparison of a nonlinear photochemical-dynamical model and lidar observations. Journal of Geophysical Research, 111, D17301 10.1029/2005JD006749

Key Points:

- Low levels of turbulence in the upper mesosphere are observed in a disturbed Arctic atmosphere following an SSW

- Low levels of turbulence coincide with low levels of gravity wave activity

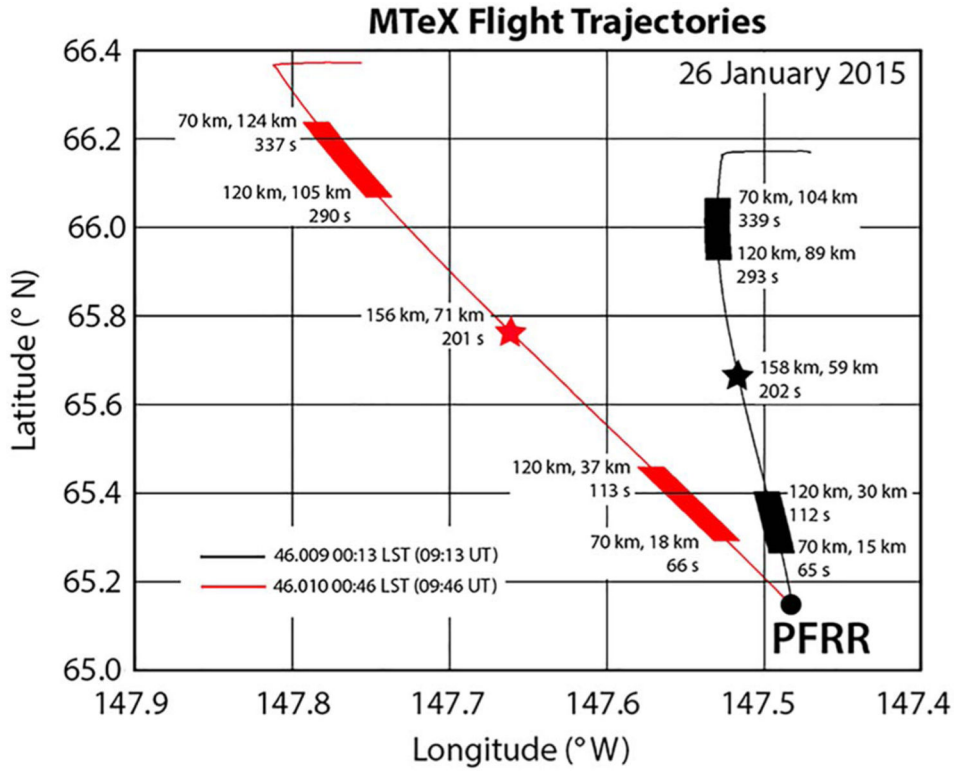- Turbulence is found in both the topside and bottomside of MILs

Figure 1.
Map of Mesosphere-Lower Thermosphere Turbulence Experiment (MTeX) flight trajectories. The trajectories are plotted as thin lines for payload 46.009 (black) and 46.010 (red). The legend includes the launch times. A black circle marks the location of Poker Flat Research Range (PFRR). The thick lines mark where the trajectory was between altitudes of 70 and 120 km. A star marks the apogee of each trajectory. Each point is labeled with its altitude, distance from PFRR, and time after launch. For example, in the upleg of 46.009 the trajectory reached an altitude of 70 km, at a distance of 15 km from PFRR 65 s after launch. At the end of their trajectories the payloads deploy parachutes and change direction as they drift to the east.
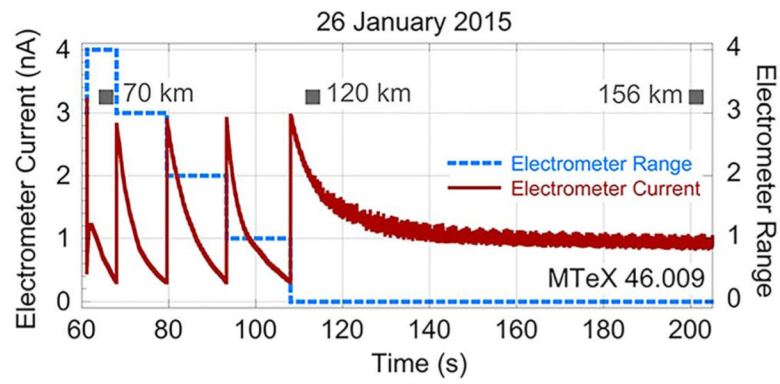
Figure 2.
Combined Sensor for Neutrals and Electrons ion-gauge electrometer current (red solid) and electrometer range (blue dashed) plotted as a function of time on the upleg of Mesosphere-Lower Thermosphere Turbulence Experiment (MTeX) payload 46.009. The altitudes of 70, 120, and 156 km (apogee) are marked for reference.
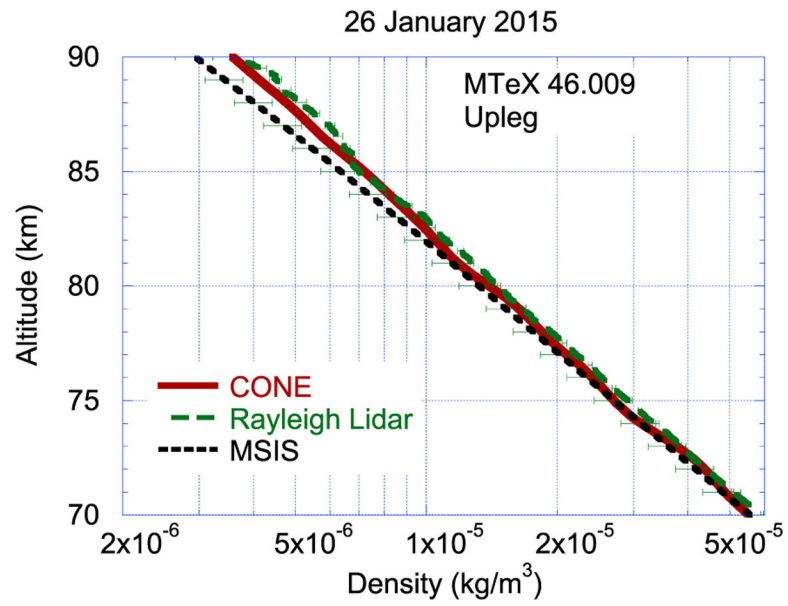
Figure 3.
Atmospheric density as a function of altitude derived from MTeX CONE ion-gauge (solid red), Rayleigh lidar (long dashed green) and MSIS (short dashed gray). The profiles are plotted with one-sigma error bars. See text for details. MTeX = Mesosphere-Lower Thermosphere Turbulence Experiment; CONE = Combined Sensor for Neutrals and Electrons; MSIS = Mass Spectrometer Incoherent Scatter.
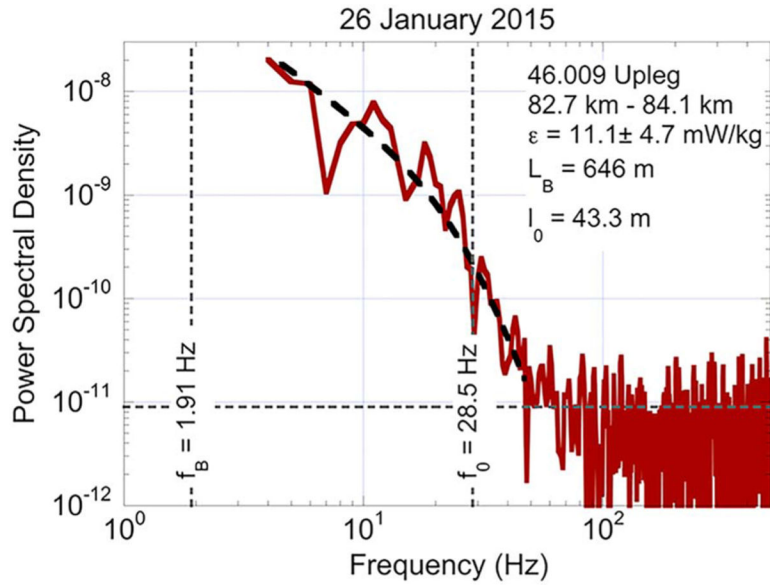
Figure 4.
Spectrum of density fluctuations derived from Combined Sensor for Neutrals and Electrons ion gauge measurements. The spectrum is plotted as solid red. The spectrum is calculated over one 1-s interval corresponding to the altitude 82.7–84.1 km. The Heisenberg model fit to the spectrum is plotted dashed black line. The background noise level is plotted as a horizontal dashed line.
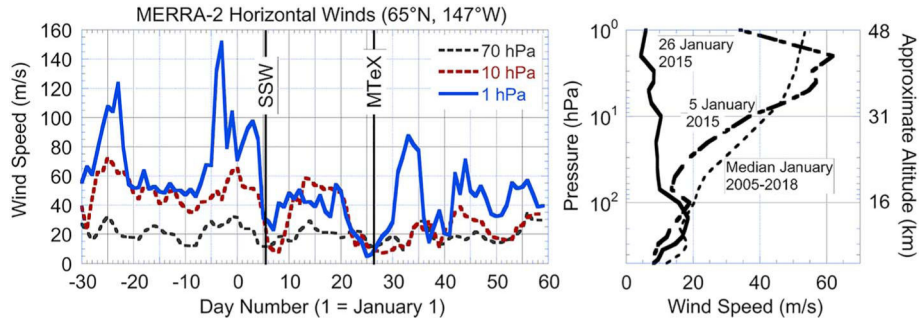
Figure 5.
MERRA-2 horizontal wind speeds over Chatanika. (left) Daily horizontal wind speed over Chatanika at 70 (~18 km, gray dashed), 10 (~31 km, red dashed), and 1 hPa (~48 km, blue solid) plotted against UT day from December 2014 to February 2015. Winds are taken at 0600 UT each day. The black vertical lines mark the dates when the SSW split the stratospheric vortex (SSW, 5 January 2015) and the MTeX launch (MTeX, 26 January 2015). (right) Vertical profile of horizontal wind on 5 January (short-long dash), 26 January (solid), and median for January 2005–2018 (short dash) plotted as a function of pressure. The corresponding approximate altitude is given on the right axis. MERRA-2 = Modern-Era Retrospective Analysis for Research and Applications version 2; SSW = Sudden Stratospheric Warming; MTeX = Mesosphere-Lower Thermosphere Turbulence Experiment.
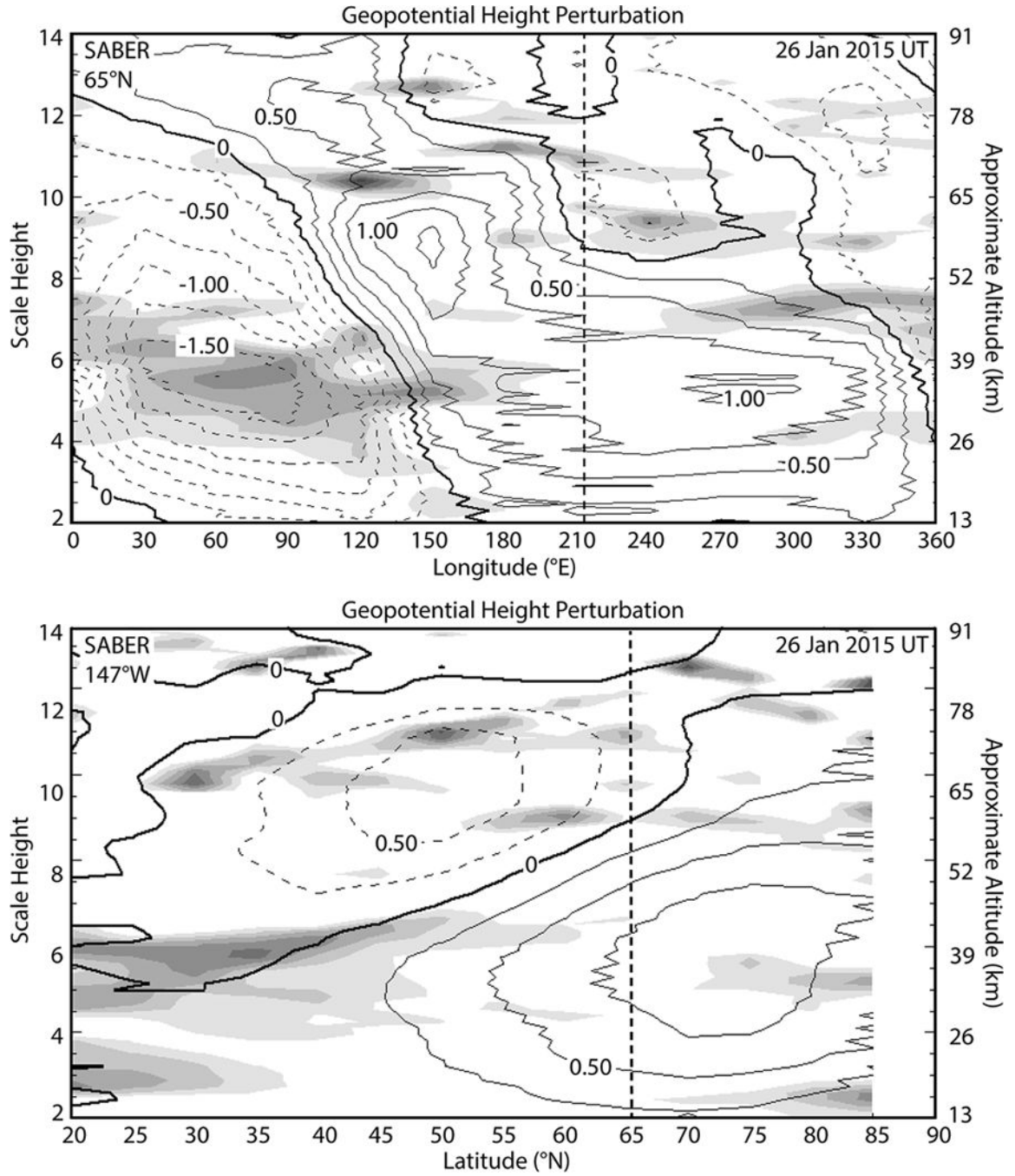
Figure 6.
Planetary wave activity derived from SABER measurements on 26 January 2015 (UT). (top)
Geopotential height perturbation and temperature gradients plotted as a function of longitude
and altitude. Geopotential contours are plotted every 0.25 km. Positive contours are plotted
solid, and negative contours are plotted dashed. Negative temperature gradients are plotted
as gray shades every 1 K/km. The shading starts at −1 to −2 K/km and progressively darkens
as the gradient becomes more negative. The location of PFRR, Chatanika, Alaska, is
indicated by the dashed line. (bottom) Geopotential height perturbation and temperature

gradients plotted as a function of latitude and altitude. SABER = Sounding of the Atmosphere using Broadband Emission Radiometry; PFRR = Poker Flat Research Range.
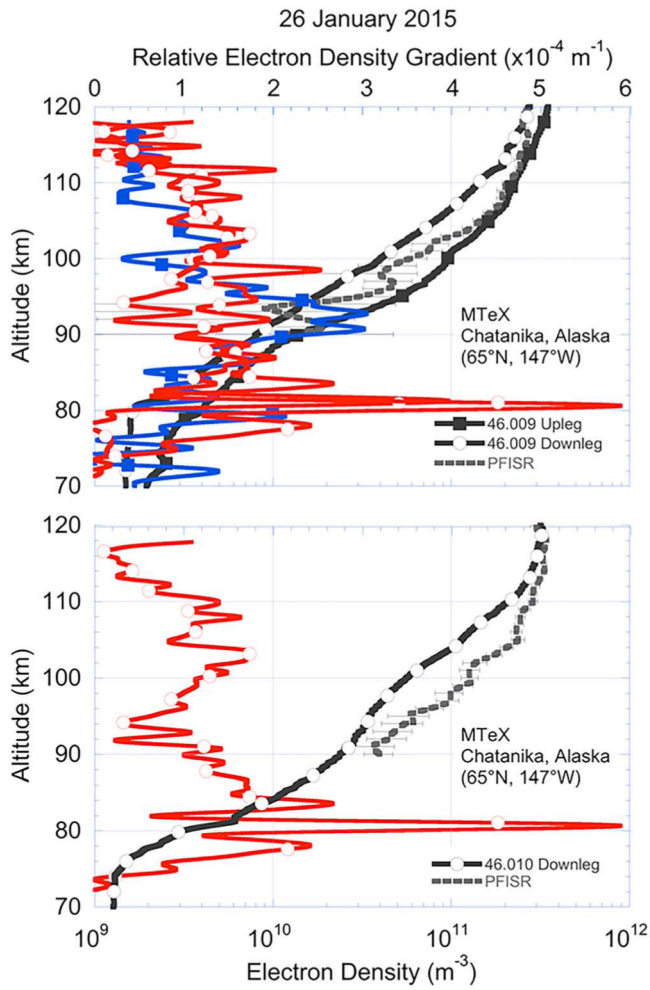
Figure 7.
Electron density (black) and relative electron density gradients (blue and read) plotted as a function of altitude for 46.009 (top) and 46.010 (bottom) payloads. The rocket measurements are plotted in solid for upleg (closed square) and downleg (open circle). The PFISR measurements are plotted as a gray dashed line. The uncertainty in the Langmuir probe measurements is 2×10^8 m^{-3} in the electron density. The PFISR profiles are plotted with one-sigma error bars. PFISR = Poker Flat Incoherent Scatter Radar.
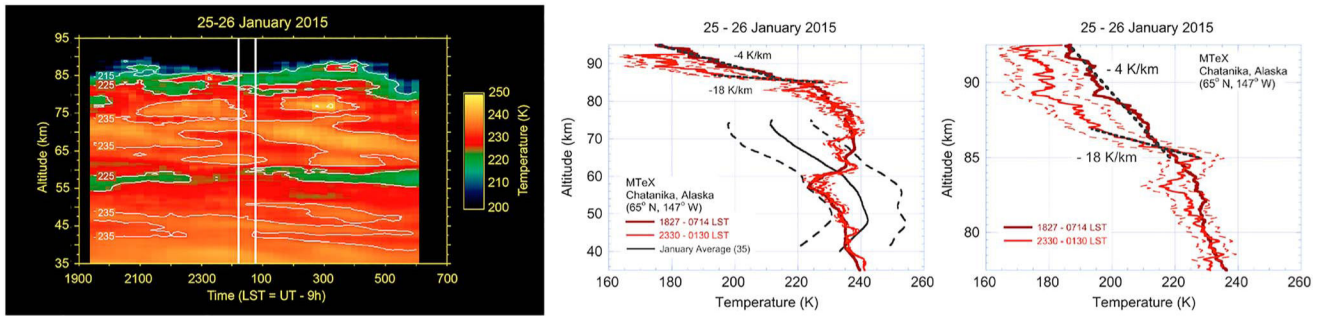
Figure 8.

Temperature derived from Rayleigh lidar measurements at PFRR on the night of 25–26 January 2015 (LST). (left) Temperature plotted as a function of altitude and time. The two vertical white lines indicate the times when the MTeX payloads were launched (46.009 at 0013 LST, 46.010 at 0046 LST). (middle) Temperature plotted as function of altitude over full altitude range of lidar measurement. Average temperature profile for the whole night (1827–0714 LST, solid red), 2-hr profile spanning the MTeX launch period (2330–0130 LST, light red), one-sigma uncertainties in 2-hr profile (light red dashed), multiyear sample mean (solid gray), and standard-deviation profile (dashed gray). (right) Temperature plotted as function of altitude over subset of lidar measurement highlighting inversion layer and superadiabatic temperature gradient. The temperature gradients of −18 and −4 K/km are indicated on the temperature profiles. PFRR = Poker Flat Research Range; MTeX = Mesosphere-Lower Thermosphere Turbulence Experiment.
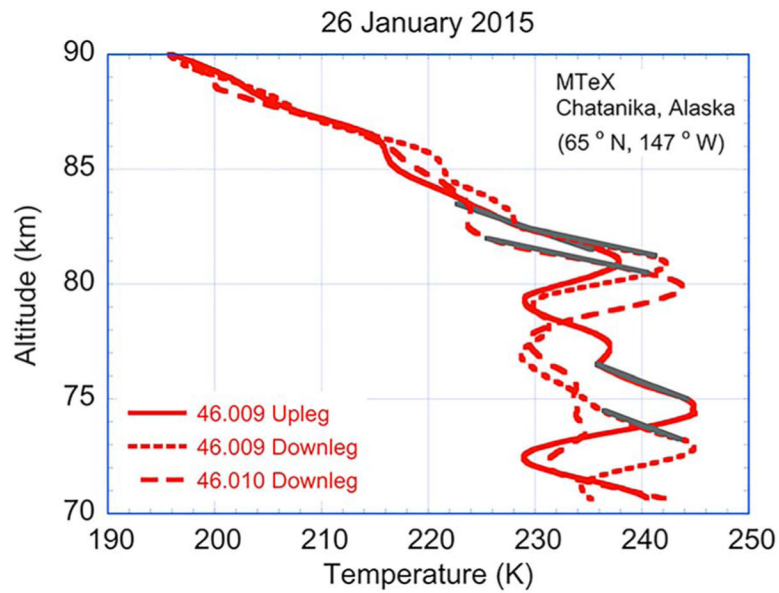
Figure 9.
Temperature derived from MTeX CONE ion-gauge measurements at PFRR on the morning of 26 January 2015 (LST). The temperature profiles are plotted in red. Temperature gradients are marked in gray. The gradients are indicated on the topside of mesospheric inversion layers near 75 and 80 km. MTeX = Mesosphere-Lower Thermosphere Turbulence Experiment; CONE = Combined Sensor for Neutrals and Electrons.
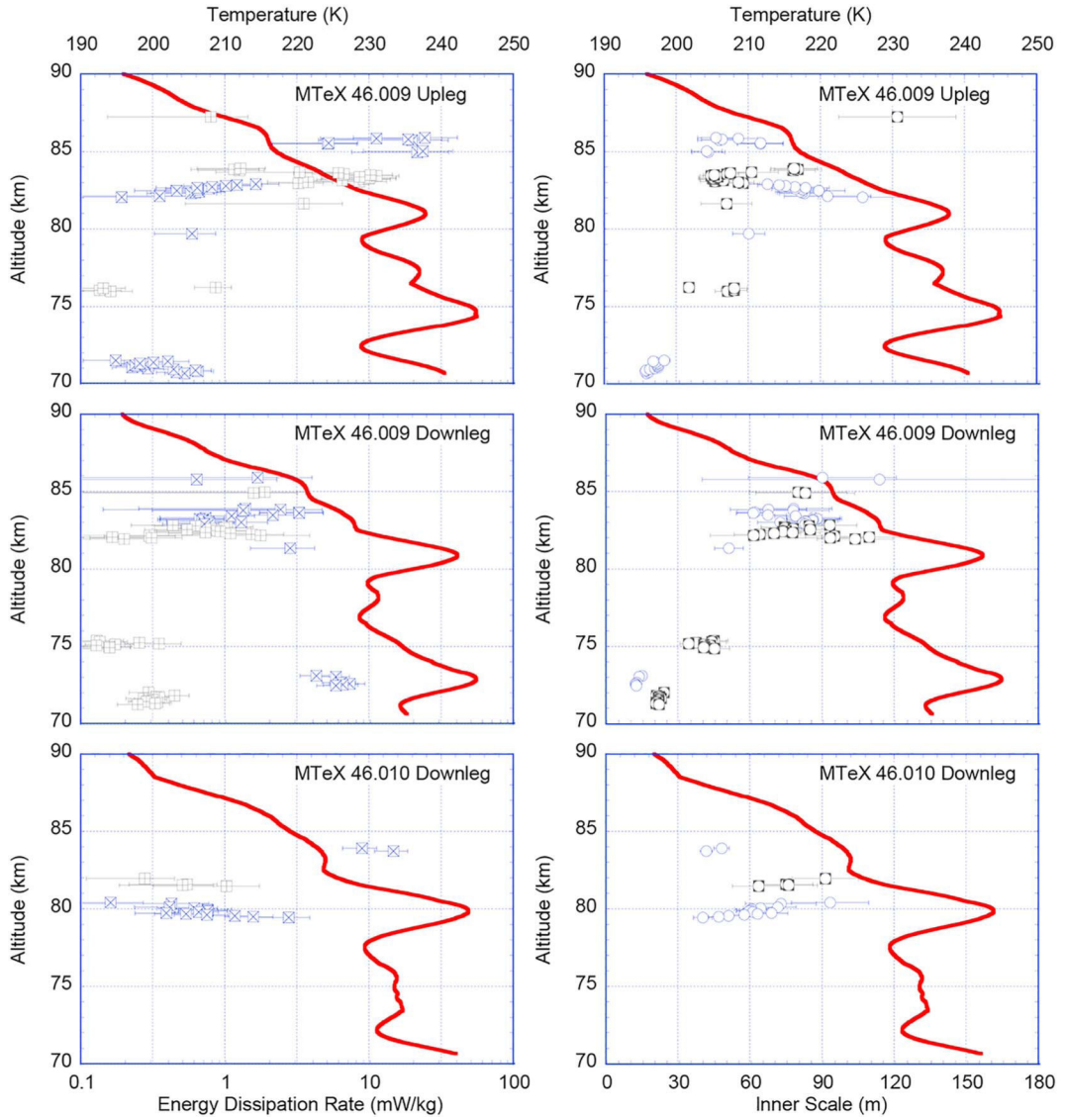
Figure 10.
Temperature (solid red), turbulent energy dissipation rate (blue square with × and black square with +), and turbulent inner scale (blue circle and black circle in square) derived from MTeX CONE ion gauge measurements plotted as function of altitude. The symbols are alternated in altitude to indicate clusters of turbulence. (top) Upleg of payload 46.009. (middle) Downleg of payload 46.009. (bottom) Downleg of payload 46.010. The turbulent quantities are plotted with one-sigma error bars. MTeX = Mesosphere-Lower Thermosphere Turbulence Experiment; CONE = Combined Sensor for Neutrals and Electrons.
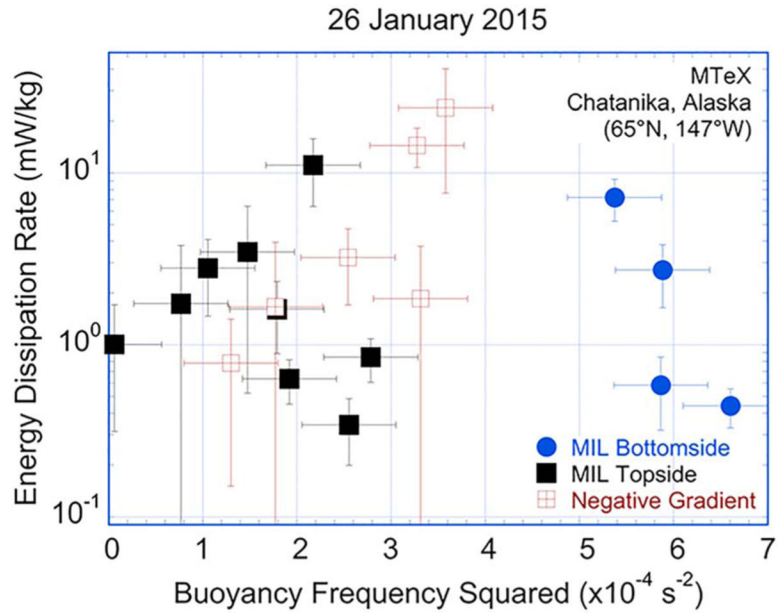
Figure 11.
Turbulent energy dissipation rate plotted as a function of buoyancy frequency squared derived from MTeX CONE ion gauge measurements. The turbulent energy dissipation rates are separated based on either the presence of a MIL or the temperature gradient; on the bottomside of a MIL (blue circle), on the topside of a MIL (black square), and where the temperature gradient is negative above the MILs (red square with +). The error bars represent one-sigma statistical uncertainties in the measurements. MTeX = Mesosphere-Lower Thermosphere Turbulence Experiment; CONE = Combined Sensor for Neutrals and Electrons; MIL = mesospheric inversion layer.
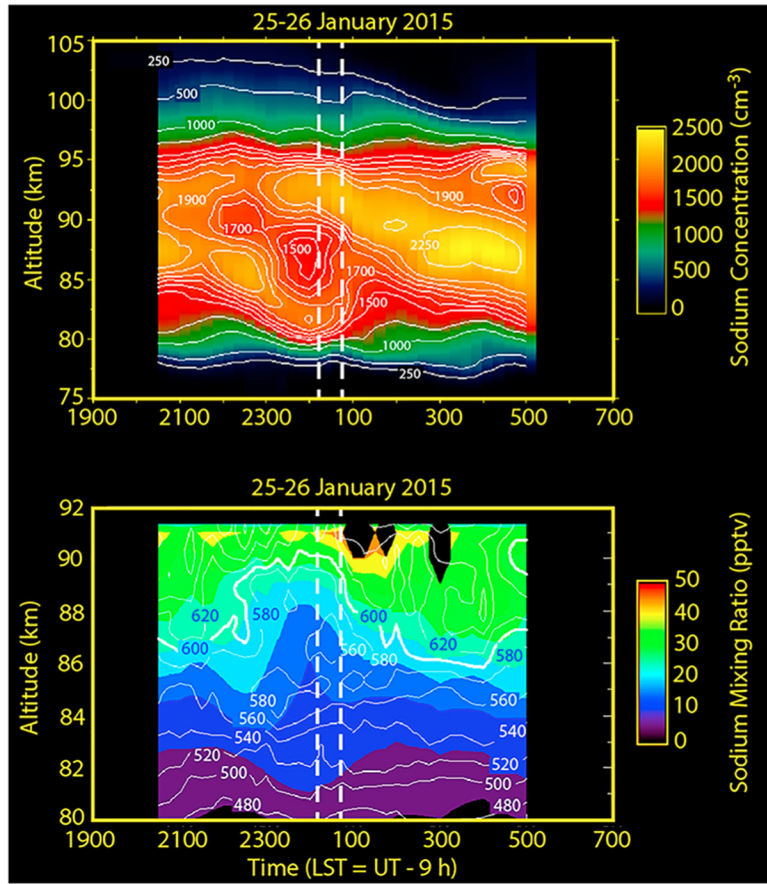
Figure 12.
Sodium and potential temperature derived from resonance and Rayleigh lidar measurements at PFRR on the night of 25–26 January 2015. (top) Sodium concentration as a function of altitude and time. The two vertical lines mark the times when the MTeX payloads were launched (46.009 at 0013 LST, 46.010 at 0046 LST). The contours are 250, 500, 1,000, 1,250, 1,500, 1,600, 1,700, 1,800, 1,900, 2,000, 2,250 cm^{-3}. (bottom) Sodium mixing ratio (false color) and potential temperature (white contour). The potential temperature is calculated starting at 61 km, and thus, the values of potential temperature are lower than if calculated from the ground level. The 600-K contour is plotted bold. The potential temperature contour labels are plotted white and blue for clarity. The two vertical dashed lines mark the times when the MTeX payloads were launched. PFRR = Poker Flat Research Range; MTeX = Mesosphere-Lower Thermosphere Turbulence Experiment.
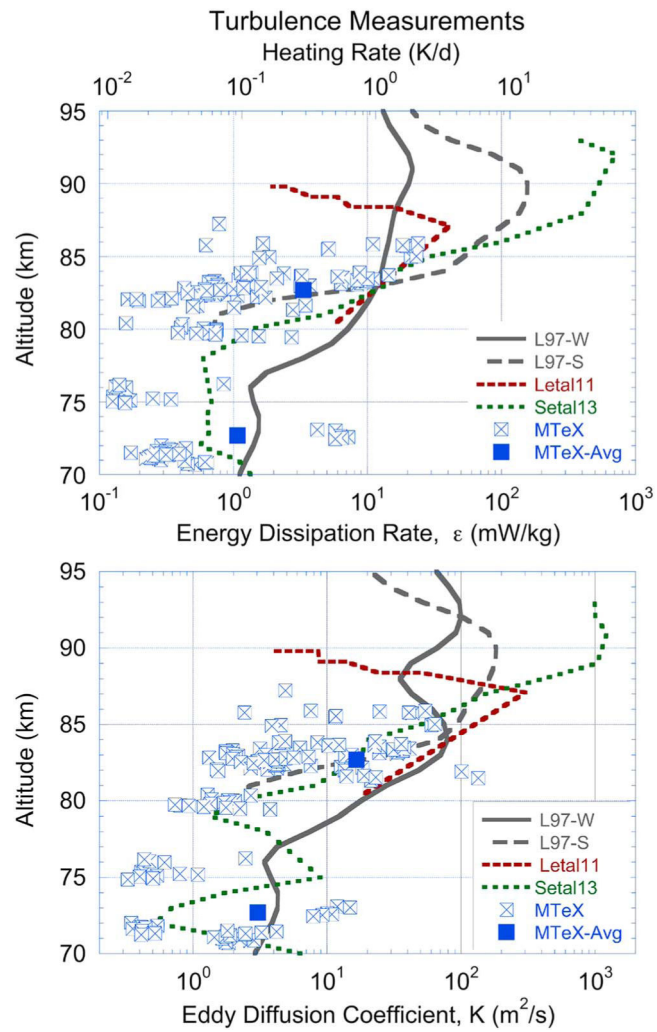
Figure 13.
Turbulent energy dissipation rate, heating rate, and eddy diffusion coefficients as a function of altitude from MTeX and other Arctic rocket-borne measurements. (top) Energy dissipation rate and heating rate. (bottom) Eddy diffusion coefficient. MTeX = Mesosphere-Lower Thermosphere Turbulence Experiment.
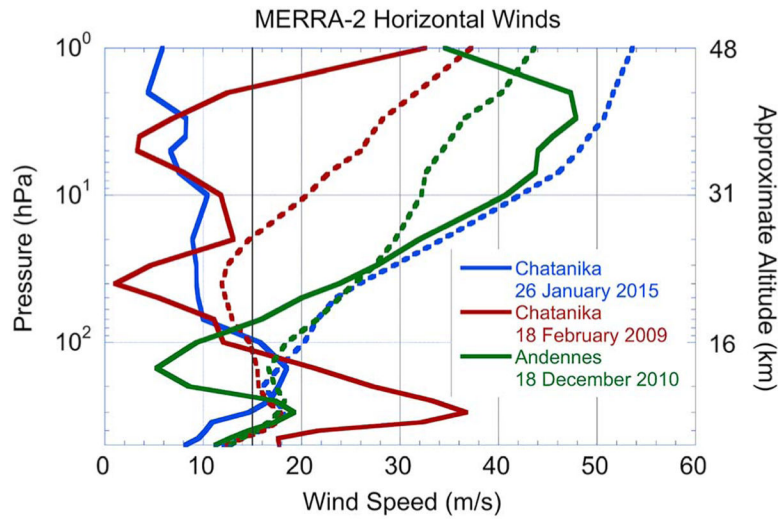
Figure 14.
Modern-Era Retrospective Analysis for Research and Applications version 2 (MERRA-2)
horizontal wind speed plotted as a function of altitude over Chatanika and Andennes. The
winds are plotted over Chatanika for 06 UT on 26 January 2015 (solid blue) and 18 February
2009 (solid red). The median winds are plotted over Chatanika for January (dashed blue)
and February (dashed red). The winds over Andennes are plotted for 18 UT on 18 December
2010 (solid green). The median winds are plotted over Andennes for December (dashed
green). The vertical gray line indicates the 15-m/s wind speed.

Table 1

MTeX 46.009 Upleg Turbulence Measurement

Turbulence	
Outer scale	646 m
Inner scale	43.3 m
Energy dissipation rate	11.1 mW/kg
Heating Rate	0.96 K/day
Eddy diffusion coefficient	41 m^2/s
Background atmosphere	
Altitude range	82.7–84.1 km
Temperature	224 K
Density	9.26×10^{-6} kg/m^3
Kinematic viscosity	1.6 m^2/s
Buoyancy period	440 s
RMS relative density fluctuation	0.08%
RMS displacement fluctuation	38 m
Data sampling	
Sampling frequency	5,208 sps
Frequency resolution	1 Hz
Rocket speed	1,234 m/s

Note. MTeX = Mesosphere-Lower Thermosphere Turbulence Experiment; RMS = root-mean-square.

Table 2

MTeX Rayleigh Lidar Measurement of Buoyancy Period and Gravity Wave Activity

Altitude range	40–50 km	37.5–52.5 km	62–67 km
Buoyancy period (s)	309 s	323 s	313 s
RMS relative density	0.26%	0.37%	0.75%
RMS vertical displacement	66 m	94 m	180 m
Specific potential energy	0.8 J/kg	1.7 J/kg	6.4 J/kg

Note. MTeX = Mesosphere-Lower Thermosphere Turbulence Experiment; RMS = root-mean-square.

Table 3

MTeX Rayleigh Lidar Measurement of Quasi-Monochromatic Gravity Waves

Measured characteristics				
Observed period	9.8 hr		2.5 hr	
Altitude range	44–51 km	63–74 km	44–50 km	64–77 km
Vertical wavelength	8 ± 4 km	12 ± 7 km	11 ± 5 km	6 ± 4 km
Relative density amplitude	0.73%	1.3%	0.36%	1.2%
Derived characteristics				
Horizontal wavelength	1270 km	1930 km	323 km	185 km
Horizontal phase velocity	36 m/s	55 m/s	36 m/s	21 m/s
Vertical group velocity	0.10 m/s	0.15 m/s	1.2 m/s	0.68 m/s
RMS horizontal velocity	6.6 m/s	11.9 m/s	1.8 m/s	6.2 m/s
Vertical displacement amplitude	179 m	322 m	88 m	299 m
Specific potential energy	6.3 J/kg	20.1 J/kg	1.5 J/kg	17.6 J/kg

Note. RMS = root-mean-square.

Table 4

MTeX CONE Measurement of Turbulence

Measurement leg	Range	Mean (median)	Range	Mean (median)
46.009 upleg				
Altitude (km)	70.7–76.2	72.2 (71.2)	79.7–87.2	83.5 (83.2)
Inner Scale (m)	16–53	26 (21)	42–121	64 (60)
Energy dissipation rate (mW/kg)	0.13–0.85	0.35 (0.28)	0.91–24	6.0 (3.4)
Points	18		40	
46.009 downleg				
Altitude (km)	71.2–75.4	73.1 (72.6)	81.3–85.9	83.1 (82.9)
Inner scale (m)	12–45	26 (22)	51 (113)	80 (79)
Energy dissipation rate (mW/kg)	0.10–7.2	1.6 (0.30)	0.16–3.2	1.2 (0.89)
Points	26		36	
46.010 downleg				
Altitude (km)	N/A	N/A	79.4–83.9	80.6 (80.0)
Inner scale (m)	N/A	N/A	40–93	63 (62)
Energy dissipation rate (mW/kg)	N/A	N/A	0.16–15	1.9 (0.69)
Points	N/A	N/A	20	
All three legs				
Altitude (km)	70.7–76.3	72.2 (71.7)	79.4–87.2	82.7 (82.8)
Inner scale (m)	12–53	26 (21)	40–121	70 (72)
Energy dissipation rate (mW/kg)	0.10–7.2	1.1 (0.29)	0.16–24	3.3 (1.0)
Points	44		96	

Note. MTeX = Mesosphere-Lower Thermosphere Turbulence Experiment; N/A = not applicable; CONE = Combined Sensor of Neutrals and Electrons.